View metadata, citation and similar papers at core.ac.uk

brought to you by CORE

provided by Explore Bristol Research

van Zalinge, M. E., Sparks, R. S. J., & Blundy, J. D. (2017). Petrogenesis of the large-volume cardones ignimbrite, Chile; development and destabilization of a complex magma-mush system. *Journal of Petrology*, *58*(10), 1975-2006. https://doi.org/10.1093/petrology/egx079

Peer reviewed version

Link to published version (if available):
10.1093/petrology/egx079

Link to publication record in Explore Bristol Research
PDF-document

This is the accepted author manuscript (AAM). The final published version (version of record) is available online via Oxford University Press at DOI: 10.1093/petrology/egx079. Please refer to any applicable terms of use of the publisher.

University of Bristol - Explore Bristol Research

General rights

This document is made available in accordance with publisher policies. Please cite only the published version using the reference above. Full terms of use are available:
http://www.bristol.ac.uk/pure/about/ebr-terms

Petrogenesis of the large-volume Cardones ignimbrite, Chile; development and destabilisation of a complex magma-mush system

Marit E. van Zalinge[1*], R. Stephen J. Sparks[1], Jon D. Blundy[1]

[1] School of Earth Sciences, University of Bristol, Wills Memorial Building, Queens Road, Clifton, Bristol, BS8 1RJ, United Kingdom

*Corresponding author: m.vanzalinge@bristol.ac.uk; 01179545366

Running title: Petrogenesis of the Cardones ignimbrite

ABSTRACT

The 21.9 Ma Cardones ignimbrite, a member of the early Miocene Oxaya Formation in northernmost Chile, is a crystal-rich (ca. 40 vol%) rhyolite with an extra-caldera thickness up to 1000 m. Access to core from eight ca. 1 km drill holes enabled sampling and petrological characterisation of pumice throughout the entire thickness of the ignimbrite at an unprecedented range of spatial scales. Mineral chemistry and modes reveal the presence of sanidine-poor and sanidine-rich pumice types, representing two, petrologically distinct magmas with the former being hotter (850-750°C) than the latter (770-670ºC). The sanidine-poor magma is amphibole-bearing and has a Ba-rich melt phase (400-1000 ppm), whereas the sanidine-rich magma has a Ba-poor melt phase (<200 ppm) and lacks amphibole. Thermobarometry of antecrystal remnants in the sanidine-poor pumice clasts indicate derivation of rhyodacitic melts from a middle crustal hot zone (950-850°C) where wet, intermediate to mafic magmas stalled and fractionated. Textures and zoning in zircon and plagioclase are consistent with the interpretation that rhyodacitic melts were episodically emplaced into the shallow crust at 6.0 to 8.7 ± 2.0 km depths over a period of ca. 200 ky. Sanidine-rich magma compositions are consistent with the melt phase in the sanidine-poor magma, hence the former could be derived by residual melt segregation from the latter. High-Ba and high-Sr zones in sanidine have compositions up to 28,000 ppm and 400 ppm respectively. Such high concentrations require input of more intermediate magmas and/or partial melting of cumulative magmas. The sanidine-rich magmas likely formed above of the sanidine-poor magmas. However, there is no systematic relationship between the different pumice types and the ignimbrite stratigraphy, suggesting major pre-eruptive destabilisation of the magmatic system led to the amalgamation and mixing of different, melt-

dominated lenses and surrounding crystal-mush to form a large heterogeneous eruptible magma body.

INTRODUCTION

The largest magnitude explosive eruptions represent hundreds to thousands of cubic kilometers of erupted magma (Dense Rock Equivalent) (Mason *et al*., 2004), which results in the deposition of widespread ignimbrites (ash-flow tuffs). Large-volume ignimbrites are commonly thought to be co-genetic with the formation of large-batholiths in the upper crust (Chmielowski *et al.*, 1999; Glazner *et al*., 2004; de Silva & Gosnold, 2007; Frazer *et al*, 2014; Ward *et al*., 2014; Lipman & Bachmann, 2015) and consequently can be used as a window into the magmatic evolution of large silicic magmatic systems (e.g. Hildreth, 1979, 1981; Chesner, 1998; Lindsay *et al*., 2001; Maughan *et al*., 2002; Bachmann *et al*., 2002; Bachmann & Bergantz, 2004; Wright *et al*., 2011; Cooper & Wilson, 2014; Willcock *et al*., 2015; Lukács *et al*., 2015; Watts *et al*., 2016).

Large-volume ignimbrites can be characterised based on their crystal content, chemical composition and compositional variations (Hildreth, 1981). Traditionally they have been classified as: 1) crystal-rich (~50 vol%) dacites that are chemically homogenous, often called monotonous intermediates (Hildreth, 1981); or 2) crystal-poor rhyolites. The latter can be divided into two subgroups (e.g. Bachmann & Bergantz, 2008): (a) cool and wet rhyolites that are commonly compositionally zoned (e.g. Bishop Tuff; Hildreth (1979); or (b) hot and dry rhyolites that lack compositional zoning (e.g. Yellowstone rhyolites). The generation of monotonous crystal-rich ignimbrites has been related to the remelting and remobilization of locked crystal mushes (>50% crystals) by heat and volatiles derived from underplating basaltic magmas (Lipman, 1997; Bachmann *et al*., 2002; Bachmann & Bergantz, 2006; Burgisser & Bergantz 2011; Huber *et al.*, 2012; Wotzlaw *et al*., 2013). In contrast, crystal-poor rhyolites have been envisaged as interstitial melt segregated from crystal-

locked mushes (>50% crystals) (Hildreth, 2004; Bachmann & Bergantz, 2004; 2008; De Silva & Gonswold, 2007; Huber *et al*., 2012). In some cases crystal-poor rhyolites can be related to crystal-rich dacites, which erupted sequentially, such as the Atana and Toconao ignimbrite, Chile (Lindsay *et al*. (2001b)).

Until recently the prevailing paradigm was that compositionally zoned rhyolites were derived from large chemically and thermally zoned magma chambers (e.g. Smith and Bailey, 1966; Smith 1979; Hildreth, 1979; Hildreth, 1981; Chesner, 1998). However, recent studies indicate that chemical and isotopic heterogeneities in crystals from crystal-poor rhyolites are compatible with magma accumulation in multiple, physically separated, melt-dominated lenses (e.g. Ellis & Wolff, 2012; Gualda & Ghiorso, 2013; Ellis *et al*., 2014; Wotzlaw *et al*., 2015) that are amalgamated shortly prior to eruption (Cashman & Giordano, 2014). There is also emerging evidence that the two ignimbrite classes do not fully represent the full diversity of ignimbrites (Fig. 7 in Watts *et al*., 2016). Crystal-rich (>35% vol% crystals) rhyolites are a third variety and examples include they Youngest Toba Tuff, Indonesia (Chessner, 1998), the Ora Ignimbrite, Italy (Willcock *et al*., 2015), and the Ceatano Tuff, USA (Watts *et al*., 2016). Another example of a crystal-rich rhyolite is the 21.9 Ma Cardones ignimbrite located in northernmost Chile, the subject of this study.

The Cardones ignimbrite is one of four major early Miocene ignimbrites known as the Oxaya Formation (Wörner *et al*., 2000), located on the Western flank of the Central Andes around the border between Chile and Peru (17-21°S). Typically these early Miocene ignimbrites have thicknesses of tens to hundreds of metres and individual volumes of up to 1500 km^3 (e.g. Wörner *et al*., 2000; García *et al*., 2004; van Zalinge *et al*. 2016). The Cardones ignimbrite is one of the largest deposits,

having thicknesses up to ~1 km (van Zalinge *et al*., 2016), covers an area of 4200 km^2 and has a minimum extracaldera volume of 1260 km^3 (García *et al*., 2004). The associated caldera has not yet been identified. The average crystal content of the Cardones ignimbrite (~40 vol%) is somewhat lower than the ~50 vol% expected for a remobilised mush. Pumice clasts have variable crystal content (32-56%), crystal proportions (sanidine-rich and sanidine-poor varieties) and trace element geochemistry (Van Zalinge *et al*., 2016). This pumice clast diversity is observed throughout a 1-km thick vertical section of the ignimbrite, meaning the Cardones ignimbrite lacks the typical systematic zonation described in, for example, the rhyolitic Bishop Tuff (e.g. Hildreth, 1979).

Our aim is to understand the petrogenesis of the Cardones ignimbrite and crystal-rich rhyolites more generally. We studied and sample multiple drill cores that penetrated the entire thickness of the Cardones ignimbrite, which enabled sampling pumice over its entire thickness and investigation of petrological heterogeneities. We present a combined modal, textural, and petrological analysis of pumices throughout the ignimbrite to understand the evolution of the magmatic system and processes leading up to eruption. Our analysis focused on minerals that preserve zoning textures and compositional variability, such as feldspars, zircon and amphibole, as these record changes in melt composition, temperature and pressure (e.g. Johnson & Rutherford, 1989; Streck, 2008; Claiborne *et al*., 2010; Cashman & Blundy, 2013). Results include crystal modes, electron microprobe analyses (EMPA) of plagioclase, sanidine, biotite and amphibole and LA-IC-MS analyses of zircon.

Our study indicates that heterogeneities in pumice clasts are consistent with the accumulation of magma (>50% melt) in at least two layers with different melt composition, crystal proportions and temperatures. These different melt-dominated

layers formed in a vertical extensive batholith-sized magmatic system, with a volume of at least a few thousand cubic kilometers, which upon eruption was extensively mixed ensuring the absence of a systematic relation between different pumice types and the ignimbrite stratigraphy.

GEOLOGICAL BACKGROUND

Deposits of the 21.9 Ma Cardones ignimbrite constitute part of the Oxaya Formation that erupted between ca. 22.2 – 19.6 Ma (Wörner *et al*., 2000; Garcia *et al*., 2004; van Zalinge *et al*., 2016). The Oxaya Formation is located on the western flank of the Altiplano (Central Andes) extending across the Central Basin, Precordillera and Western Cordillera near the border between Chile and Peru (~18°S – Fig. 1a-b). The Oxaya Formation marks the onset of large-volume ignimbrite volcanism that swept across the Central Andes and lasted until at least ca. 2 Ma (Lahsen, 1982; De Silva, 1989; Wörner *et al*., 2000a; De Silva *et al*., 2006; Salisbury *et al*., 2010; Kay *et al*., 2010; Freymuth *et al*., 2015). The large-volume ignimbrites in the Central Andes become generally younger to the south between 17° and 24°S (see compilation in Freymuth *et al*., 2015). This ignimbrite age-trend has been attributed to the southward subduction of the Juan-Fernandez ridge (Kay & Coira, 2009), which resulted in the transition from flat-slab subduction (related to subduction of the ridge) to steeper subduction. This transition in subduction regime enabled hot asthenosphere to accumulate beneath the Andean crust, giving rise to the large-volume ignimbrite volcanism (Hoke & Lamb, 2007; Kay & Cora, 2009). Between 21 and 24°S, the ignimbrites are located in the Altiplano-Puna plateau and range in age from 11 to ca. 2 Ma (De Silva, 1989). These late Miocene to Quaternary ignimbrites are co-genetic with the Altiplano-Puna magma body (Chmielowski *et al*., 1999; Zandt *et al*., 2003;

Ward *et al*., 2014; Perkins *et al*. 2016), formed in a thick crust (~70 km; James, 1971), and magma generation involved extensive crustal melting (De Silva, 1989; Kay *et al*., 2010; Freymuth *et al*., 2015). However, the geochemistry of ignimbrites to the north, including the Oxaya Formation, does not show a strong crustal signature (Freymuth *et al*., 2015) and lacks evidence for a thick, thermally mature crust at the time of magma generation (Mamani *et al*., 2010; Brandmeier & Wörner, 2016).

Stratigraphy of the Cardones ignimbrite

Based on unprecedented access to drill cores that penetrated the entire Oxaya Formation, Van Zalinge *et al*. (2016) present a detailed stratigraphy of the medial and distal deposits of the Cardones ignimbrite. The Cardones ignimbrite can be divided into two eruptive units (Fig. 1c) by a stratigraphic break and distinct welding profiles. Basal Unit 1 is found across the study area and has a thickness between 300 and 1000 m. Based on lithic and juvenile clast content Unit 1 is divided into four gradational subunits, with Subunit 1 at the base and Subunit 4 at the top (Fig. 1c). Unit 2 is only found in the eastern part of the study area (Fig 1c) with a maximum thickness of ~350 m. Unit 1 and Unit 2 have eruptive ages of 21.924 ± 0.017 (2σ) and 21.946 ± 0.012 (2σ) respectively (van Zalinge *et al*., 2016). The spread of all zircon ages for the Cardones ignimbrite is of the order of 200 ky, which is significantly greater than the uncertainties in the individual age determinations (typically less than ± 50 ky).

SAMPLES AND ANALYTICAL TECHNIQUES

Samples from the Cardones ignimbrite were collected from eight drill cores as well as from a field section in the north wall of the Lluta Quebrada (the Molinos section, Fig. 1b). This study mainly focuses on Unit 1, because drill core of Unit 2 is limited and

field outcrops were not observed. In addition, pumice clasts in Unit 2 were commonly too small or too altered to sample, whereas we sampled all subunits of Unit 1. Pumice clasts from Unit 1 had volumes in the range 10 to 70 cm^3. Thirty-seven polished thin sections of the Cardones ignimbrite were analysed; sample locations are indicated in Figure 1c (details in Supplementary Data Table 1). Samples include both bulk matrix and juvenile clasts. The Cardones ignimbrite contains <5% rhyodacitic to rhyolitic pumice clasts, typically flattened into fiamme, (Fig. 2a-b), and <<1% more mafic enclaves (van Zalinge et al., 2016) (Fig. 2c-d). The mafic enclaves have typical characteristics of more mafic magma mixed into a silicic host magma (van Zalinge et al. 2016), including rounded shapes, diktytaxitic texture and xenocrysts entrained from the silicic host. Van Zalinge *et al*. (2016) divided the rhyodacitic to rhyolitic pumice into ca. 80% crystal-rich pumice clasts (CRPs, Fig. 2a) and ca. 20% crystal-poor pumice clasts (CPPs, Fig. 2b), which are texturally different but chemically similar. In CRPs, crystals are up to 10 mm in size and range from euhedral to highly fragmented (Fig. 2e). In contrast CPPs contain only small, broken crystal fragments (≤ 1mm) that are angular to sub-rounded in shape (Fig. 2f). Van Zalinge *et al*. (2016) suggested that the CPPs were probably crystal-rich magma that was intensely sheared along feeder conduits during eruption, resulting in crystal fragmentation and resorption. The mafic enclaves are mostly andesitic in composition with a microdioritic texture (Fig. 2c); minor porphyritic dacitic enclaves occur near the base of Unit 1 (Fig. 2d).

The fragmented character of many crystals in the pumice clasts made it sometimes challenging to identify crystal zoning patterns. Phenocrysts in the mafic enclaves are typically altered. Most of the matrix consists of microcrystalline quartz

and feldspar, representing devitrified glass, which prevents accurate determination of matrix compositions.

Modal Analyses

Van Zalinge *et al*. (2016) presented crystal modes of fourteen bulk matrix samples, six CRP and three CPP clasts. We collected crystal modes of fourteen additional CRPs (Supplementary Data Table 2). Crystal modes (on dense basis) were determined using high-resolution petrographic images of thin sections in combination with the software Jmicrovision version 1.2.7 (Roduit, 2008). We used a random grid and aimed for 1000 counts per section. Sampling errors related to thin section areas and coarseness of some crystal phases are discussed in Appendix A.

Whole rock chemistry

Major and trace-element compositions of bulk rock, pumice clasts and mafic enclaves from Unit 1 were determined by inductively coupled plasma-optical emission spectrometry (ICP-OES) and inductively coupled plasma-mass spectrometry (ICP-MS) respectively. Samples from Unit 2 were too altered to perform whole rock analyses. Samples were analysed with a JY Horiba ULTIMA2 spectrometer at the Element Analysis Facility, Cardiff University, UK. The ICP-OES measurements have a relative analytical uncertainty at the 2σ confidence level of 1%, except for Fe and Na, which have a relative uncertainty of ~2%. The ICP-MS analyses have a relative uncertainty of ~5%. All analyses, with the exception of one dacitic enclave (Supplementary Data Table 3) are presented in van Zalinge *et al*. (2016). Here, the analyses of the pumice clasts and enclaves we will be further discussed and combined with petrological observations. There are significant additional errors related to the

small size of the pumice clasts and large size of some sanidine crystals. The approximate magnitude of these errors is assessed in Appendix A, using modal and grainsize data for sanidine. These errors are taken into account in interpretation of the data. Indicative calculations suggest errors of order up to 1wt% for SiO_2 content (comparable to analytical errors) and up to 1wt% for K_2O (several times analytical errors).

Mineral chemistry

EMPA were performed on plagioclase, sanidine, biotite, amphibole and minor oxide crystals. Backscatter electron (BSE) imaging was conducted to reveal compositional zoning of major crystals phases prior to EMPA, using a Hitachi S3500N scanning electron microscope (SEM) at the University of Bristol. Subsequently, the compositions of major crystal phases were measured with the Cameca SX100 5-spectrometer WDS instrument at the University of Bristol. A 20kV, 10nA beam-set up with a 1μm spot size was used to measure Si, Al, Ca, Na, K, Fe, Ti, Mg, Mn and Cl in the crystal phases (Supplementary Data Table 4). Counting times ranged from 15 to 60 seconds and Na was always measured first to minimise Na mobility. Additionally, Ba was analysed in most plagioclase and sanidine with a counting time between 60 and 120 sec. For plagioclase the typical detection limit of Ba was around 200 ppm and the standard deviation around 150 ppm. For sanidine the Ba detection limit is typically below 300 ppm and the standard deviation <400 ppm. Sr was measured in only a few sanidine crystals, using a counting time of 400 s, which resulted a detection limit below 75 ppm and a standard deviation of around 70 ppm.

Zircon grains were separated from samples 901 (Unit 1, base subunit 2, bulk), 604p (Unit 1, subunit 4 - pumice), 604 (Unit 1, subunit 4 - bulk), and 913 (Unit 2 - pumice-rich rock) (Fig. 1c). Samples were crushed in a jaw-crusher and sieved to various size-fractions. The magnetic fraction was removed from the size fractions between 50 and 250 μm. The non-magnetic sample was processed with heavy liquids LST (lithium heteropolytungstates; 2.85 g/ml) to concentrate the dense fraction. Representative zircon grains were handpicked from these fractions and mounted in epoxy. The mounts were polished to expose zircon interiors and each grain was imaged with a cathodoluminescence detector on a FEI Quanta 600 SEM at the British Geological Survey. Laser Ablation Inductively Coupled Plasma Mass Spectrometry (LA-ICP-MS) was used to measure trace-element concentrations in zircon. The analyses were performed with a New Wave Research 20 UP193-FX 193 nm ArF excimer laser on an Agilent 7500 series mass spectrometer. We analysed for P, Ca, Ti, Y, Zr, Nb, La, Ce, Pr, Nd, Sm, Eu, Gd, Tb, Dy, Ho, Er, Tm, Yb, Lu, Hf, Ta, Pb, Th and U. Glass standards 610 and 612 and zircon standard 91500 were used for calibration. The analyses were obtained with a beam fluence of 3.16 J/cm^3, irradiance of 0.64 GW/cm^2, a repetition rate of 5 Hz and a spot size of 30 μm during a 30 sec dwell time. We analysed one to four spots per zircon grain, depending on the size and zoning in the zircon. All data were processed using the program Iolite that is run over Igor pro 6.34A. The detection limit and standard deviation for each element of each analysis are given in Supplementary Data Table 5. All analyses below detection limit, as well as analyses that potentially hit inclusions, were eliminated from the dataset.

RESULTS

Modal analyses

Modal data are presented in Figure 3. CRPs contain 27 to 56 vol% crystals with the mineral assemblage containing 6-40% plagioclase, 1-16% quartz, 0-19% sanidine, 1-6% biotite, <1% titanomagnetite and 0 - 1% amphibole. Van Zalinge *et al.* (2016) showed significant modal variations in the pumice clasts, which are confirmed by the newly obtained crystal modes. A significant heterogeneity is observed in the sanidine content: in 60% of the CRPs sanidine is an abundant mineral phase (4-19 vol%), but in 40% of the CRPs sanidine is either rare (≤1 vol%) or completely absent (Fig. 3a). Table 1 presents the average crystal modes of the sandine-poor and sanidine-rich pumice clasts.

A significant issue for interpreting the modal data is that we sampled individual pumice clasts of quite small volume from the cores. Sanidine crystals, however, are large (typically in the 1 to 10 mm range) and thus there may be sampling errors related to the small size of pumice clasts relative to sanidine crystals, and the small areas sampled by individual thin sections. Consequently, we applied an analysis of sampling variance in modal values of coarse-grained rocks to verify that the observation of two types of pumice (sanidine-rich and sanidine-poor) is statistically robust. The details are provided in Supplementary Data Appendix A and the key results are presented here.

We used a stereological model of randomly distributed spheres (Lord & Willis, 1951) to reconstruct an approximate crystal size distribution of sanidines. We measured the crystal width of 70 crystals in 12 thin sections of sanidine-rich pumice clasts. We established that the sanidine crystals have a bimodal size distribution with mean sizes of 2.4 mm and 6.4 mm. Using these representative sizes we then applied a theory developed by Hasofer (1963) for sections of area A cut through randomly distributed spheres to calculate the sampling errors in the modal data. Our results

(Supplementary Data Appendix A) confirm that the two pumices clasts are drawn from different populations (a sanidine-poor and a sanidine-rich population). These populations are non-systematically distributed across the thickness of the Cardones ignimbrite (Fig. 3b). In addition our results suggest that the modal variations within the two separate populations (pumice types) can be explained by sampling errors. The modal abundance of sanidine in the sanidine-rich pumice clasts is estimated at 11.3 ± 2.7 vol%, which is consistent with the calculated average sanidine mode of sanidine-rich pumice in Table 1.

The CPPs contain between 22 and 23 vol% small broken crystal fragments, with an assemblage of 8-13% quartz, 7-12% plagioclase, 0.4-4% sanidine, <1% biotite, <1% titanomagnetite (van Zalinge *et al*., 2016). The distinction between sanidine-rich and sanidine-poor pumice in CPPs is less clear, likely due to the limited modal data available. Nevertheless, two of the CPPs are consistent with the sanidine-poor trend and one with the sanidine-rich trend (Fig 3a).

The bulk rock of Unit 1 contains on average 41 ± 9 vol% crystals (Table 1), slightly more than the crystal content of crystal-rich pumice (Table 1). In addition, bulk rock of Unit 1 always contains sanidine, between 4 and 18 vol% (Van Zalinge *et al*., 2016). In contrast, the bulk rock of Unit 2 contains 38 to 45 vol% crystals, of which <3 vol% is sanidine (van Zalinge *et al.*, 2016), significantly less than in Unit 1 (Fig. 3a).

The mafic enclaves with microdioritic texture contain mainly plagioclase and amphibole microlites (ca. 60 vol%) in groundmass and minor phenocrysts that are mostly entrained from the rhyolitic magma. Dacitic enclaves contain ~42 vol% crystals, consisting of plagioclase (~38%), amphibole (2%) and oxides (<2%) and

minor biotite in a devitrified matrix (Fig. 2d). Amphibole phenocrysts range from euhedral to rounded in shape and show reaction rims of plagioclase-pyroxene-oxide.

Whole rock major and traces element analyses

Major element data (on an anhydrous basis) of the bulk rock, pumice and enclaves of the Cardones ignimbrite have been presented in van Zalinge *et al*. (2016). Here, however, we categorized a subset of the analysed pumice clasts as either sanidine-poor or sanidine-rich (Fig. 4). Some pumice clasts were not categorized because they had already been crushed for analyses prior to the recognition of the two pumice types. From the sample set, we have excluded a strongly silicified pumice clast (sample 922) and one enclave (sample 924MD) that was silicified and contained large amounts of calcite. We recalculated the major element compositions of four pumice clasts that contained calcite. Modal content of calcite determined by point counting on BSE-images of pumice thin sections. was between 1.5 - 2 vol%. The calcite-corrected compositions are distinguished in Figure 4 by a '*'.

The sanidine-poor pumice clasts typically have SiO_2 contents <74 wt%, whereas the sanidine-rich pumice clasts have >74 wt% SiO_2 (Fig. 4). The sanidine-poor clasts show an increase in K_2O with SiO_2 (Fig. 4a). There is, however, a decrease in K_2O with increasing SiO_2 above 74 wt%. Scatter on an NaO-SiO_2 plot is attributed to high analytical uncertainties on Na measurements (Fig. 4b). The sanidine-poor pumices are enriched in CaO and TiO_2 relative to the sanidine-rich pumices (Figs. 4c and d). Consequently, major elements compositions in pumice clasts, in particular the SiO_2 – K_2O diagram (Figure 4a), indicate two different magma composition groupings, each defining distinctive trends. Trend 1 (SiO_2 < 74%) is consistent with

plagioclase control, while Trend 2 (SiO_2 > 74%) is consistent with control by sanidine + quartz.

Figure 5 presents selected trace element compositions, including Sr and Ba. We excluded all pumice clasts that show evidence for calcite alteration, due to potential for changes to the original Sr and Ba contents. Plots of Sr and Ba against SiO_2 care consistent with feldspar control, with higher Sr and Ba contents in sanidine-poor pumices compared to sanidine-rich pumices (Fig. 5a-b). Sanidine-rich pumices also have greater Eu-anomaly (Eu/Eu* = 0.5-0.6) compared to sanidine-poor pumices and the dacitic enclave (Eu/Eu* = 0.7 -1).

Normative compositions, corrected for the An-composition following the method of Blundy & Cashman (2001) are plotted on Qtz-Ab-Or ternary diagrams (Fig. 6). Pumice clasts show two main trends. Trend 1 includes the sanidine-poor pumices and plots from the Ab apex towards the 200 MPa cotectic minimum. However, the majority of the pumice clasts, including the sanidine-rich types, follow a vertical Trend 2 where the pumice clasts cluster around the eutectic-like minima at pressures between 100-300 MPa. The position of sanidine-poor pumice clasts is consistent with crystalliation of two-feldspars

Petrography and mineral composition

Plagioclase

Pumice clasts - Plagioclase crystals in pumice clasts are up to a few mm in size and commonly heavily fragmented (Fig. 7a-b). Plagioclase cores from sanidine-poor pumices range from An_{87} to An_{23} and show large variation in textures (Fig. 8a). The most calcic cores (up to An_{87}) are highly resorbed,with sieve textures. The more sodic

cores (An_{25-40}) may be replaced by more calcic (An_{50-70}) material, showing spongy textures (Fig. 7a). Plagioclase rims up to a few hundred microns thick are characterised by fine, typically normal, oscillatory zoning. The outer-most rim compositions are typically around ~An_{30} (Table 2). Plagioclase inclusions in amphibole and biotite have compositions of An_{27-53} (n=36) and An_{29-51} (n=9) respectively.

Most plagioclases from sanidine-rich pumices are weakly oscillatory-zoned or unzoned with compositions <An_{30} (Fig. 7c). However, some sanidine-rich pumice clasts also contain plagioclases with core textures and compositions similar to those described in the sanidine-poor pumices (Figs. 7d). Nevertheless, the outermost rims of all analysed plagioclase crystals in sanidine-rich pumices are more sodic than the plagioclase in sanidine-poor pumices, specifically between An_{25} and An_{23} (Fig. 8b, Table 2). Plagioclase found as inclusions in, or intergrown with sanidine have compositions between An_{21-35} with an average of An_{24} (n=90) (Fig. 8d).

Ba-concentration in plagioclase varies from 900 ppm to below the detection limit (bdl) of ~200 ppm (Fig. 8a and b). Ba is incompatible in plagioclase, although the partition coefficient for Ba increases with the Ab content of plagioclase (Blundy and Wood, 1991). A decrease in Ba at low An-contents suggests depletion of Ba in the melt due to co-crystallisation of a phase in which Ba is compatible, such as sanidine and/or biotite. Figure 8a shows that Ba is inversely correlated with An-content for plagioclase analyses greater than An_{30}. However, for analyses that are more sodic than An_{30}, Ba is bdl. Typically, plagioclase rims of sanidine-poor pumice clasts have Ba concentrations between 500 - 700 ppm at ~An_{30}, and plagioclase rims of sanidine-rich pumices contain Ba bdl at ~An_{25}. In addition, plagioclase inclusions in sanidine contain relatively less Ba compared with inclusions in biotite and

amphibole (Fig. 8d), which is consistent with sanidine crystallizing after amphibole and biotite. The Ba-concentrations in plagioclase can be used to estimate the Ba concentration in the melt in which the plagioclase grew. Using the Ba partition coefficient expression from Blundy & Wood (1991), we find that plagioclase (An_{45-30}) in sanidine-poor pumice clasts crystallised from melts that contained between 1000-400 ppm Ba. In contrast, the plagioclase ($<An_{30}$) in sanidine-rich pumice clasts crystallised from melts that contained <200 ppm Ba.

Overall, the plagioclase data indicate that plagioclase co-crystallised with amphibole and preceded sanidine and biotite crystallisation, with sanidine crystallisation initiating when plagioclase reached a composition around An_{30}.

Dacitic enclave - Plagioclase crystals in the dacitic enclave are euhedral. Half of the plagioclase cores as well as minor rims exhibit sieve textures that are in-filled by alteration products. All plagioclases exhibit fine oscillatory zoning with compositions around An_{50-70} and a Ba-content bdl (Fig. 8c). The outermost rims of the plagioclase are a few tens of microns wide and are more sodic in composition ($<An_{40}$) (Table 2). The rims contain 600 to 1000 ppm Ba, suggesting the melt contained up to 1200 ppm Ba during this final growth stage (Table 2).

Mafic enclaves with microdioritic textures - Microdiorites contain euhedral plagioclase microlites up to 300 μm in size that are normally zoned with An_{40-50} cores and An_{25-35} rims. Microdiorites also contain plagioclase phenocrysts with resorbed cores (An_{40-25}) overgrown by ~100 μm wide normally-zoned (An_{55-25}) rims (Fig. 8c). These textures suggest that these phenocrysts originally crystallised in more silcic magmas and were subsequently entrained into the andesitic host magma. The Ba

composition of plagioclase microlites increases from ca. 200 ppm to 400 ppm with An-content decreasing from An_{50} to $An_{35.}$ Microlites from one micodiorite have Ba-depleted rims of ~An_{25}.

Quartz

Euhedral quartz crystals up to 5 mm in size occur in both sanidine-rich and sanidine-poor pumices. Anhedral quartz crystals that are either rounded or exhibit melt embayments are also observed in both pumice types. Within a single sanidine-poor or sanidine-rich pumice, euhedral quartz and quartz with embayments co-exist. Resorption of quartz indicates either (1) decompression, which shrinks the quartz phase volume in the Qtz-Ab-Or diagram (Fig. 6) or (2) mixing with a hotter less-evolved magma.

Sanidine

Sanidine occurs in sanidine-rich pumices and all studied bulk rocks. It is commonly euhedral and tabular in shape. Grain size is bimodal (Appendix A) with modes around 2.4 and 6.4 mm and crystal sizes reaching up to 10 mm (Fig. 9a-c). Sanidine compositions range from Or_{73} to Or_{60}. Variation in Or-content in a single crystal is typically limited to a few mol%. Bulk rock samples from the base (subunit 1) and top (subunit 4) of Unit 1, as well as Unit 2 mainly contain sanidine between Or_{70-73}. Analyses from the middle section of Unit 1 (subunit 2 and 3) are more variable in composition (Or_{60-71}) with a tendency to lower Or giving an overall parabolic profile of sanidine compositions through the ignimbrite (Fig. 10).

Ba is compatible in sanidine with partition coefficients between 2 and 32 (Ren, 2004). Partitioning of Ba into sanidine depends on melt composition as well as

sanidine Or- and An-contents (e.g. Ginibre *et al*., 2004; Ren, 2004; Zellmer & Clavero, 2006). Sanidines in the Cardones ignimbrite contain between 1000 and 28,000 ppm Ba. Figure 9a-d show various types of Ba zoning in sanidine: Type 1 crystals are unzoned or weakly zoned with Ba <15,000 ppm (Fig 9a); Type 2 crystals contain high-Ba zones (Ba >15,000 ppm) in the outer core and inner rim (Fig. 9b); Type 3 crystals commonly exhibit resorption of the core and have a high-Ba (>15,000 ppm) outer-most rim (Fig. 9c). The high-Ba zones in type 2 and 3 sanidines are relatively enriched in Sr (≤400 ppm) compared to low-Ba zones.. Types 1 and 2 can be found in sanidine-rich pumices and the bulk rock of Unit 1. About 10% of the analysed crystals from the Unit 1 bulk rock contain at least one zone with >15,000 ppm Ba.. In contrast, Type 3 crystals are most common in matrix samples from Unit 2 and about 50% of the crystals analysed in this unit contain a zone with >15,000 ppm Ba.

Biotite

Biotite occurs in all pumice clasts and throughout the bulk ignimbrite and can be up to 5 mm in size. Bent and kinked biotites are common (Fig. 11a) and alteration to chlorite and magnetite is observed along cleavage planes. Plagioclase (An_{28-51}) and apatite are the most common inclusion phase. Biotite shows only minor variations in chemistry (Fig. 11b-c). Biotite from sanidine-poor pumices has slightly lower Mn (~0.5) concentrations than those from the sanidine-rich pumices (~0.8). Rare, highly altered biotites in the enclaves are attributed to entrainment from the rhyolitic magmas.

Amphibole

The sanidine-poor pumices and bulk rocks contain less than 2 vol% amphibole crystals. Amphibole is absent from sanidine-rich pumices, with the exception of a single altered crystal in one pumice clast. The dacitic enclave contains 2 vol% amphibole crystals with thick plag-pyroxene-oxide reaction rims and common magnetite inclusions (Fig. 12a). Most amphibole in sanidine-poor pumices and bulk rock is sub-euhedral, and reaction rims are common (Fig. 12b and c). Twenty-one amphiboles were analysed in 7 different samples, including sanidine-poor pumice, bulk-rock and the dacitic enclave (Table 3). The procedure of Holland & Blundy (1994) was used to calculate the amount of ferric iron and to determine atoms per unit formula.

The total Al-content (Al_{tot}) in amphiboles shows a bi-modal distribution with peaks at Al_{tot} 1.15 and 2.0 (Fig. 12d). The low-Al_{tot} crystals are typically Mg-hornblendes and the high-Al_{tot} crystals are mainly Mg-hastingsite (Leake *et al*., 1997). All amphiboles are plotted in Figures 12e and 12f, and typical core and outermost rim analyses are shown in Figures 12g - 12i. In general Al_{tot} shows a positive correlation with Al_{vi}, Ti and Na+K. Two different core to rims trends are recognised on a plot of Al_{tot} versus Mg# (Figs. 12f and i). In Trend I, Mg# is negatively correlated with Al_{tot} over a gradual trend. In contrast, Trend II is characterised by crystals that show a step in Al_{tot} from core to rim at constant Mg#. Amphiboles from the dacitic enclave typically plot at the high-Al_{tot} end of Trend II, while bulk rock and pumice clasts contain amphiboles that plot along both trends. Unaltered amphiboles have outermost rim compositions with 0.84 to 1.16 an Al_{tot}.

Magnetite is a common inclusion in most amphibole. Plagioclase (An_{30-53}) inclusions are common in high-Al_{tot} amphiboles that plot along Trend I. Trend II high-Al_{tot} amphiboles, however, lack plagioclase inclusions, suggestive of water-rich

magmas in which plagioclase crystallization is suppressed. Biotite and plagioclase (An_{27-46}) inclusions are common in low Al_{tot} amphiboles.

Titanomagnetite

Subhedral titanomagnetite (<500μm) is common in the pumice glass matrix and is commonly associated with biotite and both high-Al_{tot} and low-Al_{tot} amphiboles. All crystals exhibit prominent exsolution and oxidation features. Only a single magnetite-ilmenite pair was found in the matrix rock. This pair, as well as a few exsolved titanomagnetites, were analysed to obtain an average composition of the oxides to use for crystal fractionation modelling (Table 4).

Accessory phases

Apatite and zircon are the most common accessory phases in the Cardones ignimbrite. Two allanite crystals were observed, one in the matrix rock and one in a sanidine-rich pumice. Apatite occurs as prismatic crystals, typically <100 μm in size, in matrix glass and as inclusions in biotite, magnetite and amphibole.

Zircon - Zircon occurs as euhedral, doubly-terminated prismatic crystals with aspect ratios commonly <5:1 (Fig. 13a). Crystals are sometimes broken and fractured. Zircon textures are dominated by fine, oscillatory zoning (Fig. 13b) and commonly contain melt and small apatite inclusions. About 20% of the investigated zircon cores exhibit resorption features with overgrowth of rims. Half of the resorbed cores are much darker in CL-images than non-resorbed cores and rims, with less obvious oscillatory zoning (Fig. 13b, grain 2_913_M).

The complete dataset of zircon analyses can be found in Supplementary Data Table 5. Trace-element analyses of zircons from both Units, as well as from pumice and bulk rock exhibit the same trends. Therefore we grouped the analyses by crystal location (i.e. core vs. rim) rather than by sample. Spidergrams for all analysed zircons show a positive Ce-anomaly and a negative Eu-anomaly (Fig. 13c). Zircons are enriched in HREE relative to LREE; core and rim analyses show a similar range in REE elements. Hf concentrations range from 8,000 to 17,000 ppm (Fig. 13 and g), with the majority of zircon cores clustering at <10,000 ppm, except for a small group of resorbed dark cores with 12,000 to 17,000 ppm. Rim analyses are more equally distributed over the full Hf range. The Hf concentration in zircon is commonly used as an indicator of differentiation, where higher Hf concentrations are associated with more evolved melts (e.g. Claiborne *et al.,* 2006, 2010; Hoskin & Schaltegger, 2003). The Eu-anomaly (Eu/Eu*) of the zircons shows a negative correlation with Hf (Fig. 13d), consistent with feldspar crystallisation. Resorbed zircon cores with Hf >12,000 ppm are extremely enriched in incompatible elements such as U (Fig.13) and Th. The partition coefficient of U and Th typically increases with decreasing temperature, reaching values up to 200-400 and 50-100, respectively, at temperatures below 800°C (review by Claiborne *et al*., 2010).

Yb/Gd characterises the variation of HREE/MREE in the zircons (Fig. 13f) with a positive, albeit scattered, correlation with Hf. In particular, Yb/Gd increases from 10 to ~25 at Hf concentrations between 8000 and 11,000 ppm. At Hf >11,000 ppm, Yb/Gd is constant around 25 ± 5. Yb/Gd increases from 10 to ~25 at constant Eu/Eu* values of ~0.5. In contrast, the main decrease in Eu/Eu* (from ~0.5 to 0.1) occurs at relative constant Yb/Gd values of 25 ± 5. Variations in Yb/Gd are commonly attributed to amphibole crystallisation (Cooper *et al*., 2014). These

observations therefore suggest that during zircon crystallisation, plagioclase crystallisation was dominant with minor to negligible amphibole crystallisation.

Ti content in the zircons is negatively correlated with Hf (Fig. 13g). Nevertheless, for a single Hf concentration, Ti concentrations can vary over a range of 7 ppm, which exceeds the ±2 ppm analytical uncertainty of Ti. Yb/Gd values are not correlated to the Ti concentration (Fig. 13h).

TEMPERATURE

Plagioclase-amphibole thermometry

Temperature was calculated for thirty-six plagioclase-amphibole pairs in ten different amphiboles in the sanidine-poor pumices and bulk matrix (e.g. Fig. 12b-c). Thermometers A and B of Holland & Blundy (1994) were applied (Supplementary Data Table 6). In Figure 14, we present the results of thermometer A for the low-Al_{tot} (1.0 - 1.4 apfu) amphiboles in the quartz-bearing Cardones pumice clasts, as this thermometer is designed for Si-saturated rocks. It is, however, unclear whether the high-Al_{tot} ($\geq$ 1.5 apfu) amphibole cores grew in the presence of quartz and thus for these crystals we present the results of thermometer B (Fig. 14a). Temperatures range from 873 to 722°C and decrease with the decreasing Al_{tot}. Note that no temperatures were calculated for the high Al_{tot} amphiboles that plot along the Trend II in Figures 12f and 12i, due to the absence of plagioclase inclusions.

Zircon saturation temperatures

We calculated the zircon-saturation temperatures using the model of Boehnke et al., (2013), which is a development of the model by Watson & Harrison (1983). The model requires input of the Zr concentration as well as the cation ratio

(Na+K+2Ca)/(Si*Al) of the melt. We used the Cardones pumice clasts as a proxy for the Cardones melt (as we do not have any matrix glass analyses) and excluded all samples showing evidence of alteration. As the Cardones melt was zircon-saturated (zircon is an abundant accessory mineral in pumice clasts) the calculated values provide maximum zircon-saturation temperatures (Miller *et al*., 2003). We calculated temperatures between 675 and 787°C, with 90% of the temperatures falling between 765 and 715°C (Fig. 14). These temperatures are lower than those calculated for the high-Al_{tot} amphibole-plagioclase pairs, but partly overlap with the temperatures for the low-Al_{tot} amphibole-plagioclase pairs.

Ti-in-zircon thermometry

In order to apply the Ti-in-zircon thermometer, appropriate values for silica and titanium activity must be chosen (Ferry & Watson, 2007; Watson & Harrison, 2005; Watson *et al*., 2006). The Cardones ignimbrite contains significant amounts of quartz thus $a SiO_2 \approx 1$. The $aTiO_2$ is thought to be ≥0.6 in silicic systems that, like the Cardones ignimbrite, lack rutile (Hayden & Watson, 2007). Therefore we calculate the Ti-in-zircon temperatures with $0.6 < aTiO_2 < 0.8$, using the formulation of Ferry & Watson (2007). This range of $aTiO_2$ confers a temperature variation of ±28°C at 750°C.

Ti concentration in zircon ranges from 16.5 to 3 with an estimated typical error of ≤ 2ppm (2σ) (Supplementary Data Table 5). Note that some analyses are below the detection limit of 2 ppm. The thermometer yields temperatures from 840 to 655°C ($\alpha TiO_2 = 0.6$), 830 to 645°C ($\alpha TiO_2 = 0.7$) and 820 to 635°C ($aTiO_2 = 0.8$) (Fig 13f). An analytical uncertainty of 2 ppm Ti translates to errors of -23, +30 at $aTiO_2 = 0.7$. Figure 14 shows that both rims and cores have the same variation in

temperature. Moreover, the temperature variation in resorbed and unresorbed cores is similar. The high-end range of the Ti-in-zircon temperatures overlap with the zircon saturation temperatures and the low-Al_{tot} amphibole-plagioclase temperatures. In contrast, the Ti-in-zircon temperatures are lower than those calculated for the high-Al_{tot} amphiboles.

Zircons with the same Hf concentrations show a temperature spread of up to 100°C (Fig. 13g). This temperature difference can be even larger (up to 150°C) for a fixed Yb/Gd concentration (Fig. 13h). These temperature differences exceed the 2σ analytical uncertainty of the Ti-in-zircon thermometer, which are -23, +30, at αTiO_2 = 0.7. Thus melts with similar trace-element budget could have been at markedly different temperatures.

Two-feldspar thermometry

Temperatures were also calculated from coexisting sanidine and plagioclase pairs from sanidine-rich pumices and the bulk matrix. We targeted plagioclase inclusions in sanidine (e.g. Fig. 9a-c) or intergrown mineral pairs and analysed the compositions 5-10 μm from the grain boundary. Before calculating the two-feldspar temperatures, we tested eight different thermometers (Ghiorso, 1984; Green & Usdansky, 1986; Nekvasil & Burnham, 1987; Fuhrman & Lindsley, 1988; Lindsley & Nekvasil, 1989; Elkins & Grove, 1990; Putirka, 2008) to assess which two-feldspar thermometer gives the most reliable results for potassium feldspar- and plagioclase-bearing experiments on silicic systems at known pressure and temperature that were not used to calibrate any of the thermometers.. Data were taken from Scaillet *et al*. (1995); Klimm *et al*. (2003); Almeev *et al*. (2012); and Bolte *et al*. (2015) (Supplementary Data Table 6).

We used the software SOLVALC by Wen & Nekvasil (1994) to calculate the temperatures for most thermometers, except for the Putirka (2008) thermometers.

The results of the two-feldspar thermometry test are given in the Supplementary Data Table 6 and Appendix B. The majority of the thermometers overestimate the temperatures (by up to a few hundred degrees), especially at temperatures above 800°C. The performance of most thermometers improved below 800°C. The thermometer of Fuhrman & Lindsley (1988) best reproduces the experimental temperatures, with an average misfit of 25°C (supplementary material). At temperatures <750°C the average misfit is reduced to 17°C.

We calculated 50 temperatures using 23 sanidine-plagioclase pairs, which were either plagioclase inclusions in sanidine or intergrown feldspar pairs, using the Fuhrman & Lindsley (1988) formulation. For each calculation we used pressures of 150, 200 and 250 MPa and assigned an uncertainty of 2 mol% to the measured An, Or and Ab (Supplementary Data Table 6). Temperatures for the different pressures vary less than the calculated uncertainty of 25°C, and therefore we only present the 200 MPa results. We calculated temperatures between 780°C and 655°C (Fig. 14). The low-end of the calculated temperatures cluster around the granite solidus at water saturation for pressures between 200-500 MPa (Johannes & Holtz, 1996). The highest calculated temperature is similar to the results of the 200 MPa Fish Canyon Tuff experiments (Caricchi & Blundy, 2015). Those experiments show that sanidine begins to crystallize below 780°C and 775°C for experiments with 4 wt% H_2O and H_2O-saturated, respectively. Or-content in sanidine is a sensitive parameter in the two-feldspar thermometer. Thus, the highest temperatures are calculated for sanidine with the lowest Or-content (Fig. 10). The two-feldspar temperatures overlap the low-end

temperature range of the Ti-in-zircon thermometer, but are lower than amphibole-plagioclase temperatures, in good agreement with the observed crystallisation order.

PRESSURE AND H_2O-CONTENT

The lack of melt inclusions in Cardones pumices rules out using volatile-saturation pressures to constrain magma storage depths. Instead we have used the compositions of Cardones amphiboles, in conjunction with experimental studies to constrain crystallization pressures. Because amphibole composition is sensitive to both intensive parameters and bulk composition, we carefully selected nine experimental studies performed on starting compositions similar to the amphibole-bearing sanidine-poor pumice clasts and dacitic enclaves (Naney, 1983; Johnson and Rutherford, 1989; Schmidt, 1992; Scaillet & Evans, 1999; Proteau & Scaillet, 2003; Cadoux *et al*., 2014; Riker *et al*., 2015; Mutch et al., 2016; Blatter *et al*., 2017) (Supplementary Data Table 7). For this limited compositional range, the experimental amphiboles show a good correlation between Al_{tot} content of amphibole and pressure (Fig. 15). The correlation is non-linear, flattening out above 400 MPa. Scatter reflects the variation in experimental temperature, which also influences Al_{tot}, and variability in the buffering capacity of the coexisting mineral assemblage. Nonetheless, we can use Figure 15 to provide insights into the crystallization pressures of Cardones amphiboles.

The high-Al_{tot} amphiboles associated with Trend II (Fig. 15) are consistent with pressures above 400MPa that correspond to crystallisation in the middle to lower crust (>15 km depth). At these pressures amphibole is stable at temperatures <950°C and water contents typically >4 wt% (Prouteau & Scaillet, 2003). Furthermore, the lack of plagioclase inclusions included within the Trend II high-Al_{tot} amphibole in

some samples is consistent with amphibole preceding plagioclase in the crystallisation order. Experimental data on granodiorites show amphibole crystallisation preceding plagioclase crystallisation at 800 MPa and an H_2O content >5wt% (e.g. Naney 1983). In contrast, Trend I high-Al_{tot} amphiboles co-crystallised with plagioclase and give temperatures around 850°C. The strong relation between Trend I amphiboles and temperature suggests (Fig. 14a) that the high Al_{tot} end of this trend is attributable to elevated temperature rather than higher pressure.

We calculated the pressures for low-Al_{tot} amphiboles using the newly calibrated formula for Al-in-amphibole barometer of Mutch *et al*. (2016). The outermost rims of unaltered low-Al_{tot} amphibole have Al_{tot} content between 0.84 and 1.16, which yield pressures from 150 to 220 ± 50 MPa, corresponding to a depth range of 6 to 8.7 ± 2 km (for a crust with density 2600 kg/m^3). A requirement for this barometer, however, is that the amphibole was in equilibrium with the buffering assemblage of biotite, plagioclase, potassium feldspar, quartz, magnetite, ilmenite, and apatite. There is no direct evidence that amphibole crystallised with sanidine, which might affect the results. Nevertheless, experiments on synthentic granodiorites at 200MPa (Naney, 1983) indicate that an assemblage of plagioclase + hornblende + biotite + liquid is stable at between 780 - 750°C at H_2O-content >5 wt%, consistent with our calculated temperatures for the plagioclase- low-Al_{tot} amphibole pairs.

The sanidine-rich pumice cluster near the 200 MPa cotectic minimum on the Qtz-Ab-Or ternary diagram (Fig. 6). In addition, experiments by Naney (1983) on synthetic granites indicate that at 200 MPa a mineral assemblage of plagioclase + K-feldspar + quartz + biotite + liquid is present between 750 and ~680°C and bulk H_2O-content ranging from 1 to 10 wt%, which is in agreement with the 2-feldspar temperatures.

Further constraints on crystallization pressures for the sanidine-rich pumices are provided by recent experiments on a Cardones rhyolite, reported by Mutch et al (2016) and Tattitch & Blundy (2017). Although these experiments were not designed as phase equilibrium runs, they afford insights into the variation of mineral assemblage with pressure. A single 810 °C, 100 MPa run (CMA201) in Mutch et al. (2016) produced amphibole + biotite + plagioclase (An_{42}) + sanidine + oxides + quartz + apatite + clinopyroxene in equilibrium with water-saturated melt (5.3±1.4 wt% H_2O). Tattitch & Blundy (2017) performed experiments on the same Cardones starting material at 100 and 200 MPa and 810 °C and 725 °C. They note that clinopyroxene is lacking at 200 MPa, and that, at 200 MPa, sanidine disappears between 725 and 810 °C (only relict grains were observed at the higher temperature). The absence of clinopyroxene from Cardones pumices is therefore indicative of pressures above 100 MPa. The presence of sanidine in the sanidine-rich Cardones pumices requires temperatures below 810 °C; its scarcity in sanidine-poor pumices is suggestive of temperatures at or above 810 °C. These conditions are in good agreement with those estimated for the low Al_{tot} amphiboles, and suggests that sanidine-poor pumices containing amphibole crystallised at slightly higher temperatures than sandine-rich pumices lacking amphibole

SUMMARY OF MAIN RESULTS

The Cardones magmas were rhyodacitic to rhyolitic, albeit with minor (<<1% of total volume) andesitic and dacitic enclaves (Fig. 2). Petrographic observations in combination with EMPA of minerals within pumice clasts established the crystallisation sequence of the Cardones magmas (Fig. 16a). Four sets of observations indicate that at least two petrologically distinct magmas erupted (Fig. 16b). Firstly,

modal analyses (Fig. 3, Table 1) recognize two pumice types (Fig. 16b). Sanidine-poor pumice clasts contain on average 37 ± 9 (1σ) vol% crystals with an assemblage of plagioclase > quartz > biotite > titanomagnetite > amphibole > sanidine (sanidine commonly absent). Sanidine-rich pumice clasts containing on average 36 ± 7 (1σ) vol% crystals with an assemblage of plagioclase - sanidine - quartz > biotite > titanomagnetite (amphibole absent). Secondly, the compositions of plagioclase, in particular their rims, in these two pumice types differ (Fig. 8a-b). Rims in sanidine-poor pumice clasts are characterized by An_{30} and ~550 ppm Ba, whereas rims in sanidine-rich pumice are typically An_{25} and have Ba compositions below the detection limit of 200 ppm. Hence, we infer that the melts of the sanidine-poor magma contained significantly more Ba (400-1000 ppm) than the melts in the sanidine-rich magmas (<200 ppm Ba). Thirdly, Mn in biotite is slightly lower in the sanidine-poor (~0.5 apf) pumice compared to the sanidine-rich pumice (~0.8 apf). Finally, the temperatures of the sanidine-poor magma were higher than those of the sanidine-rich magma. Plagioclase-amphibole thermometery performed on crystal-pairs in the sanidine-poor pumice clasts give temperatures between 850-750°C (Fig 14a), whereas 2-feldspar temperatures performed on crystal-pairs in the sanidine-rich pumice clasts give temperatures between (770-670°C). These temperature differences are consistent with published phase equilibrium experiments on a Cardones rhyolite. Normative compositions plotted on a Qtz-Ab-Or ternary diagram (Fig. 6b) and experimental data are also consistent with the sanidine-poor magmas being hotter than the sanidine-rich magmas. Barometry and mineral assemblages (notably the absence of clinopyroxene) indicates both magmas resided at pressures around 150 to 220 ± 50 MPa. We now discuss the origin of and relationship between the various magma batches.

DISCUSSION

Deep origin of the Cardones magma

The Cardones magmas are predominantly rhyodacitic to rhyolitic in composition (at least 1260 km^3, based on volume estimates by García *et al*., 2004). Amphibole barometery indicates that these silicic magmas resided in the shallow crust (6 to 8.7 ± 2 km depth) prior to eruption. However, comparison of the high-Al_{tot} amphiboles in the dacitic enclave and sanidine-poor pumice clasts with experimental data (Fig. 15), indicates that these silicic magmas were generated at pressures >400MPa, which corresponds to depths >15 km (middle crustal levels), Similar depths are determined for the late Miocene-Pliocene intermediate lavas of the Aucanquilcha Cluster located 250 km to the south of the study area (Walker *et al*., 2013). Annen et al. (2006) referred to a middle to deeper crustal zone in which silicic magma is produced as a hot zone.

The lack of plagioclase associated with the Trend II high-Al_{tot} amphibole is consistent with the interpretation that amphibole preceded plagioclase in the crystallisation order, which requires a H_2O content >5wt% at 800 MPa (e.g. Naney, 1983). Hence, our preferred mechanism is that the rhyodacitic melts were generated by amphibole-dominated fractionation from wet mafic magma that stalled in a middle-lower crustal hot zone. Amphibole fractionation in the deeper crust is also consistent with the marked MREE depletion relative to HREE and LREE in the Cardones sanidine-poor pumice, whereas these pumices only have a small Eu-anomaly (Eu/Eu* = 0.7 – 1) (van Zalinge *et al*., 2016). These interpretations are consistent with an isotopic study by Freymuth *et al.* (2015) that calculated that only 20% of the Oxaya Formation magmas can be attributed to crustal assimilation, while

the remainder is related to magma differentiation and perhaps remelting of juvenile material. The absence of garnet signature in the trace-element contents of the Cardones magma suggests the thickness of the crust in the early Miocene was not as great as the present-day crustal thickness (Mamani *et al*., 2010; Brandmeier & Wörner, 2016).

It is challenging to infer the exact composition of the magmas from which the silicic melts were generated. Andesitic and dacitic enclaves demonstrate more mafic magmas in the system. Plagioclase with calcic core compositions (>An_{80}) suggest involvement of mafic magmas, noting that such calcic plagioclases cannot be precipitated from dacitic magmas at pressures up to 960 MPa (Proteau & Scaillet, 2003). Conversely, Laumonnier et al (2017) provide experimental evidence to show that andesitic magmas from nearby Cerro Uturuncu volcano, crystallise $An_{>80}$ plagioclase at pressures of >500 MPa and dissolved H_2O >8 wt%. We interpret the high-An plagioclase and the high-Al_{tot} amphiboles either as antecrysts entrained by disruption of mafic cumulates during transfer of the rhyodacitic melts from their source regions (e.g. Walker *et al*., 2013), or by mixing of these silicic magmas with porphyritic mafic magmas. The resorption of both the high-Al_{tot} amphiboles and the high-An plagioclase can be explained by near-adiabatic ascent of magmas to the shallow crust (Annen *et al*., 2006; Prouteau & Scaillet, 2003). Evidence for deeper crustal processes is predominantly found in the sanidine-poor pumice clasts. Hence we infer that the magmas feeding into the shallow reservoir were predominantly rhyodacitic in composition with a minor andesitic-dacitic component (Fig. 17). Temperatures of Cardones magmas in the hot zone source are estimated from amphibole stability (e.g. Naney, 1983; Proteau and Scaillet, 2003) and the plagioclase-high-Al_{tot} amphiboles thermometry, and hence constrained at 950-850°C.

These conditions are strikingly similar to those inferred for the Altiplano-Puna Magma Body by Laumonnier et al (2017).

Although zircon crystallisation took place in the shallow crust, trace element data indicate variations in the compositions of the melts acquired at greater depth prior to onset of zircon crystallisation. In particular, variations in Yb/Gd in zircon reflect variations of the same ratio in the melts. Yb/Gd variations in melts are a hallmark of amphibole crystallisation, but amphibole is a minor component of the sanidine-poor magmas (Table 1). Furthermore Yb/Gd ratios in zircon are poorly correlated with the zircon temperatures (Fig. 13h) and Hf concentrations (Fig. 13f). These observations are not consistent with co-crystallisation of zircon and amphibole in the shallow silicic magmas. Yb/Gd variations are thus attributed to a cryptic and variable amphibole fractional crystallisation (Davidson *et al*., 2007; Smith, 2014) in the middle-crustal hot zone (Annen *et al*., 2006) prior to transfer to the shallow crust.

Emplacement of melts in the shallow crust

In the section above we discussed that composition of the magma feeding into the shallow magma reservoir was likely rhyodacitic in composition (sanidine-poor magma type). Recharge of large volumes of silicic magma from depth is a common feature for such large silicic systems and has been documented in many deposits, including A.D. 1600 Huaynaputina eruption, Peru (de Silva *et al*., 2008); the Cerro Galan ignimbrite (Wright *et al*., 2011), and the Minoan eruption, Santorini (Druitt *et al*., 2012). High-precision, whole-grain zircon ages for the Cardones ignimbrite span ~200 ky (van Zalinge *et al*., 2016). This range is significantly greater than the uncertainties in the individual age determinations (typically less than ± 50 ky). The significant spread in zircon dates within a single sample is consistent with the

hypothesis that large silicic magmatic systems grow incrementally by episodic magma flux from depth over time-scales on the order of 10^5-10^6 years (Matzel *et al*., 2006; De Silva & Gonswold, 2007; Reid, 2008; Schoene *et al*., 2012; Wotzlaw *et al*., 2013; Cooper *et al*., 2014; Frazer *et al*., 2014; Eddy *et al*., 2016; Reid & Vazques, 2016). In this conceptual model the shallow pluton grows in short-lived bursts with long, intervening dormant periods, which is supported by the typical episodic character of silicic volcanism and pluton growth (Annen, 2009; Annen *et al*., 2015). Thermal models of such episodically growing magmatic systems show several regions of melt-dominated magma (<50% crystals) that are surrounded by larger volumes of mush (>50% crystals) (Annen, 2009). We found multiple lines of evidence, outlined below, that are in agreement with this replenishment scenario.

Firstly, the resorption and disequilibrium features observed in the Cardones zircons are consistent with those found in large silicic bodies that spend a significant part of their lifetime as a crystalline-mush (e.g. Claiborne *et al*., 2010; Lukács *et al*., 2015; Reid & Vazques, 2016). Ti-in-zircon thermometry and zircon-saturation temperatures (Fig. 14) indicate that the shallow magma-mush system spent much of its time at temperatures <800°C. Resorption textures require the interaction of zircons with zircon-undersaturated melt, which could be caused by magma mixing with hotter less-evolved melt. Amphibole-plagioclase temperatures indicate that some of the Cardones magmas were, at times, hotter than the calculated zircon-saturation temperatures (Fig. 14b), implying that magma interactions could have led to transient generation of zircon-undersaturated melts. Resorbed zircon cores have the most evolved trace-element signatures (Fig. 13; e.g. high Hf, high U, most negative Eu-anomaly), indicating that these zircons formed in highly evolved melts. The resorbed cores are typically overgrown by rims with a less-evolved trace-element character

(e.g. Fig. 13). These zircon textures can be interpreted in two ways, both consistent with an open magma-mush system. Firstly, they could represent crystal mush that contained small pockets of highly evolved residual melt along with zircons that was subsequently remobilised and recycled by the input of replenishment magma (e.g. Huppert & Sparks, 1988; Claiborne *et al*., 2010) or heat derived from underlying replenishment magma (Couch et al. 2001). Specifically, remobilisation of mush at the margins of a growing magma body results in initial resorption followed immediately by crystallisation of overgrowth rims as initially resorbed crystals are swept into the interior of the cooling magma body (Huppert & Sparks, 1988). This explanation is in line with interpretations for the Uturuncu Volcano, Bolivia (Muir *et al*, 2014) where large heterogeneities in trace elements from matrix glass are related to local differences in apatite crystallisation/resorption in separate melt pockets within a locked crystal mush. Alternatively, these highly evolved zircon-saturated magma layers could have segregated from mush by compaction (Jackson *et al*., 2003; Solano *et al*., 2012), and subsequently mixed with zircon-undersaturated magma after which the hybrid magma cooled and crystallised. Zircons with no obvious resorption textures are typically normal-zoned, which can be explained simply by progressive cooling and crystallisation of the magmas (e.g. Fig. 13d).

Resorption textures in plagioclase crystals also support an open magma-mush system. Plagioclase in the sanidine-poor magmas are typically characterised by compositions between An_{50-30} (Fig. 8a). Some plagioclase crystals, however, show multiple zones with compositions $>An_{50}$ (e.g. Fig. 7a), which are commonly associated with reactive dissolution textures. Such textures develop when a crystal is in equilibrium with a more An-rich melt (i.e. hotter, wetter or more mafic) than the melt in which the crystal is entrained (Tsuchiyama, 1985; Blundy & Shimizu, 1991;

Cashman & Blundy, 2013). One explanation is that these textures can develop when the replenishment magma either interacts chemically and/or thermally with slightly older, colder and more evolved magmas in the shallow magma reservoir (e.g. Cashman & Blundy, 2013; Couch et al. 2001). Release of latent heat during decompression crystallisation of water-saturated newly arrived magma may provide an additional source of heat to cause resorption (Blundy *et al*, 2006) as can variation in volatile fluxes (e.g. H_2O and CO_2; e.g. Blundy & Cashman, 2013; Riker *et al*., 2015). Finally, resorbed plagioclase cores could also represent xenocrysts that were entrained and resorbed as magma ascended through the mush regions of the system (Annen *et al*., 2006).

Processes in the shallow magmatic system; origin of sanidine-rich magma

Whereas sanidine-poor pumice clasts provide evidence for a deep crustal origin, the sanidine-rich pumice clasts originate from magmas with compositions close to the granitic minimum (Fig. 6) crystallized at shallow levels (~200 MPa). We now investigate to what extent the sanidine-poor and sanidine-rich magmas could be related via crystal fractionation processes, including melt segregation.

Interpretation of major element trends

Figures 4 and 6 show trends in major elements within both sanidine-poor and sanidine-rich pumice clasts. These trends can be explained by controls of the major mineral phases, notably plagioclase, quartz and sanidine. Interpreting the trends, however, is not straightforward since both sampling artifacts and igneous processes could reproduce them. For the sanidine-poor pumice data crystal size is not an issue (modal size ~ 1-2 mm) so the trends are attributed principally to igneous processes. In

Figure 6a, Trend 1 plots away from the Ab apex, which implies dominant plagioclase control. The same trend could be induced by fractional crystallisation or magma mixing of heterogeneous magmas originating in the deeper hot zone. However, the large size of some sanidines makes interpretation of Trend 2 in sanidine-rich magma more problematic (as discussed in Supplementary Data Appendix A). Trend 2 is consistent with fractional crystallisation of two-feldspars, but could also be influenced by variability in the proportions of sanidine crystals sampled from the magma by individual pumice clasts.

Crystallisation modelling

We performed least squares regression modelling for the major oxides, using the program MINSQ (Herrmann & Berry, 2002) to investigate whether sanidine-poor and sanidine-rich pumices are related by crystallisation processes. We used the least squares regression method to solve the equation: Parent composition = Daughter composition + crystal assemblage. To choose parent compositions, we selected seven least evolved pumice clasts, which plot almost in the same position in major element diagrams (Fig. 4; Table 4) (we excluded pumice clasts that showed evidence for alteration.) These pumices include the sanidine-poor samples and plot along Trend 1 in the Qtz-Ab-Or ternary diagram (Figs. 4a and 6a). To determine the daughter composition, we averaged the compositions of thirteen sanidine-rich pumice clasts that plot along Trend 2 (Fig. 6). Using an average composition is justified as Trend 2 is likely influenced by sampling artefacts (Supplementary Data Appendix 2), rather than crystallisation. We selected representative crystal compositions (including: plagioclase, quartz, biotite, amphibole, magnetite, ilmenite and sanidine) from the sanidine-poor pumices. We found that the daughter composition could be derived

from the parent compositions by 24 to 42wt% crystallization (Table 4).. The average normalised mineral percentages are: 59% plagioclase (An_{40}), 26% quartz, 7% biotite, and 4% titanomagnetite, 2% sanidine, 2% amphibole. These results match closely the average, normalised mineral mode of the sanidine-poor pumice clasts (in wt%): 64% plagioclase, 20% quartz, 10% biotite, 3% titanomagnetite 1% amphibole, <1% sanidine. Thus, the sanidine-rich magma composition is consistent with the composition of the melt phase in the sanidine-poor magma and therefore the former could have been derived by residual melt segregation from the latter.

We also performed Rayleigh fractionation and equilibrium crystallisation modelling (e.g. Tindle & Pearce, 1981) with the trace elements Ba, Sr and Rb. These three elements are the most informative; as they are strongly controlled by crystallisation of the major mineral phases in the Cardones ignimbrite. We used mineral-melt partition coefficients from Blundy & Wood (1991), Ewart & Griffin (1994) and Ren (2004) (Table 5). To find an appropriate starting compositions, we took the same parental pumice compositions to those in the least squares regression model: Sr = 246 ± 40 ppm, Rb = 115 ± 16 ppm and Ba = 890 ± 140 ppm (1σ). We then used the average crystal modes for sanidine-poor pumice to perform the calculations (Table 5) and compared the results with the trace-element budget typical for sanidine-rich pumices (Sr = 138 ± 18; Rb = 151 ± 16; Ba = 606 ± 111 (1σ)) Equilibrium modeling provides a good fit with the data for most parent compositions (results of sample 505RF presented in Fig. 5c-d) and indicates about 20-50% crystallisation is required to move from a trace-element budget typical for sanidine-poor pumices towards a trace-element budget typical for sanidine-rich pumice. Rayleigh fractionation requires about 20% crystallization, but does not yield a good match the average composition of sanidine-rich pumices.

Plagioclase rims in sanidine-rich and sanidine-poor magmas are distinct. Nevertheless, plagioclase cores from both pumice types show compositional overlap, which could be attributed to common histories of the two magmas. In particular, sanidine-rich pumice clasts contain plagioclase with cores between An_{50-30} that are typical for plagioclase in sanidine-poor pumices. If the sanidine-rich magma is extracted as evolved melt from the sanidine-poor magma then the cores in the former can be interpreted as antecrysts entrained from the latter magma during segregation.

Crystallisation modeling indicates that the sanidine-poor and sanidine-rich magmas could be related via crystallisation. Nevertheless, as indicated in earlier sections, shallow crustal processes, such as crystal fractionation, likely occurred in an open system. Consequently, some of the heterogeneities that are related to fractionation processes may instead reflect the input of heterogeneous magmas from deeper crustal levels.

Ba-zoning in sanidine

The crystallisation model indicates that extracted melt from the sanidine-poor magma contains up to ca. 700 ppm Ba (Fig 5d). This is consistent with the plagioclase compositions in the sanidine-poor pumices that indicate the melts had Ba contents ranging from 1000 to 400 ppm Ba. Ren (2004) suggests that the partition coefficient for Ba in sanidine could range from 2 to 32. By taking an average partition coefficient of 17, one can expect Ba-zones in sanidine up to 12,000 ppm for melts with ~700 ppm Ba, consistent with the Ba contents of most sanidine. However, 10% and 50%, respectively, of the sanidine crystals in Unit 1 and Unit 2 contain Ba-zones between 15,000 and 28,000 ppm Ba. These high Ba-zones are also enriched in Sr (≤400 ppm)

compared to the low-Ba zones (Fig. 9b and c). Using a partition-coefficient of 4 for Sr in sanidine (Ren, 2004), these melts would have contained 1600 ppm Sr.

One explanation for high-Ba-zones in sanidine is that a less evolved melt with high Sr and Ba content mixed with the sanidine-rich magma. The admixed melt may correspond to the more dacitic-andesitic magmas found as enclaves in the rhyolite. These more mafic enclaves in the Cardones ignimbrite, however, contain <600 ppm Ba and Sr, concentrations that are too low for the high-Ba-rims in sanidine (Fig. 5a-b). A more extended data-set on mafic enclaves collected from the Quaternary Taapaca volcano directly east of our study area indicate that dacitic magmas with Sr and Ba contents up to 1400 and 1500 ppm respectively were generated in the crust (Blum-Oeste and Wörner, 2016). Such high-Sr and -Ba may also been present in the Cardones system and could easily have crystallised sanidines with high-Ba and -Sr rims. An alternative explanation is that these high-Ba and Sr melts were generated by melting feldspar-rich cumulates or cumulative magmas (mush-piles) by recharge magmas (Bachmann et al., 2014; Wolff et al., 2015). Melting plagioclase and sanidine (and biotite) would increase both Sr and Ba concentrations in the melt. This process could explain the resorbed sanidine with high Ba-overgrowth rims (Fig. 9 – Type 3 sanidine), which is a commonly observed in Unit 2 (Fig. 9c). These features are absent in Unit 1 and so the stratigraphic relationships are consistent with the presence of cumulative magmas in the lower part of the system.

Model for the Cardones magmatic system

Figure 17 illustrates the proposed model for the Cardones magmatic system. We envisage that predominantly dacitic to rhyodacitic melts were generated in the middle and lower crust and ascended to the shallow crust (6 to 9 ± 2 km). These melts had the

signature of cryptic amphibole fractional crystallisation and entrained antecrysts formed at higher temperature and pressure within the hot zone. The distinct characteristics of sanidine-poor and sanidine-rich pumice types demonstrate the presence of two petrologically distinct magmas with the former magma being higher in temperature (850-750°C) than the latter (770-670ºC). Because the second eruptive unit (Unit 2) of the Cardones ignimbrite contains much less sanidine than the first eruptive unit (Fig. 3a), we infer that the cooler sanidine-rich magma was developed above the hotter sanidine-poor magma. This model is consistent with the interpretation that melts segregated from the sanidine-poor magmas to form the sanidine-rich magma body at the top of the system. This is similar to the model for the generation of the Toconao ignimbrite in Chile (Lindsay et al., 2001).

Mineral chemistry data indicate that the two magma types were internally heterogeneous in composition and temperature. Variations of Or-content in sanidine throughout the Cardones ignimbrite can be explained by temperature variation of about 100°C within the sandine-rich magma (Fig. 10). The zircon data show variations in zircon temperature, Hf and Eu/Eu* (Fig. 13), indicative of a heterogeneous system containing melts that had experienced various degrees of feldspar-dominated fractionation (Claiborne *et al*., 2010; Chamberlain *et al*., 2013; Cooper & Wilson, 2014). Chemical heterogeneities in crystals have been found in many other large volume ignimbrites (e.g. Chesner, 1998; Maughan *et al*., 2002; Wright *et al*., 2011; Cooper *et al*., 2012; Ellis and Wolff, 2012; Gualda and Ghiorso, 2013; Ellis *et al*., 2014; Wotzlaw *et al*., 2015).

Our data are inconsistent with the idea that large crystal-rich ignimbrites are defrosted and remobilized crystal-locked mushes, driven by upward migrating heat and volatiles derived from underplating mafic magmas to form large, homogenous,

well-mixed bodies of eruptible magma (e.g. Bachmann *et al*., 2002; Bachmann & Bergantz, 2006; Burgisser & Bergantz, 2011; Huber *et al*., 2012). Observations that have led to the defrosting model include high crystal content, monotonous composition, complexly zoned crystals, reverse-zoned crystals (e.g. amphibole and zircon), and abundant resorbed anhydrous crystal phases (e.g. Lipman *et al*., 1997; Bachmann *et al*., 2002; Bachmann & Dungan, 2002; Wotzlaw *et al*., 2013). The Cardones ignimbrite, however, shows limited petrological evidence for large-scale reheating and remelting of a crystal mush. Resorption textures in sanidine, plagioclase, and zircon are observed, but these are uncommon and thus more consistent with local remobilization of a crystal mush and/or cumulates by replenishment magma from depth. Secondly, amphiboles show a decrease of $Na+K_a$ from core to rim (Fig. 12g) that is attributed to declining temperatures (e.g. Blundy & Holland, 1990), and also the rims of plagioclase crystals are typically normal zoned. Finally, the distinct pumice types and associated temperatures suggest limited chemical and thermal mixing of the magmas prior to and during the eruption of the Cardones magmatic system.

Catastrophic destabilisation event

The even distribution of different pumice types through ~1000 m section of Unit 1 of the Cardones ignimbrite (Fig 3b and van Zalinge *et al.*, 2016) reveals no systematic relation between the compositional variation and ignimbrite stratigraphy. We suggest that the co-eruption of at least two different magmas implies a major disturbance of the magmatic system, rather than systematic tapping of the separate magma bodies as indicated for the Atana and Tonocao ignimbrites by Lindsay et al. (2001). We infer instead that eruption was preceded by a large-scale, catastrophic destabilisation of the

magmatic system (Fig. 17). Destabilisation led to amalgamation and mixing of the different magma batches with some of the surrounding crystal mush/cumulates (Cashman & Giordano, 2014). Rare pumice clasts with crystal content >50 vol% could represent relicts of erupted mush. The presence of distinct pumice types with their own preserved magmatic temperatures indicates limited chemical and thermal homogenization of the magma, suggestive of short timescales. Hence, we suggest that catastrophic destabilisation and amalgamation occurred shortly before and/or during the eruption.

There is no direct evidence for the triggering mechanism(s) that caused the catastrophic destabilisation and subsequent eruption of the Cardones ignimbrite. Replenishment by new silicic magma generated at depth, as envisaged by de Silva *et al*. (2008), could have triggered destabilisation. Replenishment by silicic magmas shortly before eruption has also been proposed for the large-volume Cerro Galan ignimbrite (Wright *et al*., 2011) and the Toba Tuff (Reid and Vazquez, 2016). Other possible triggers are spontaneous destabilisation of the system without replenishment due to the growth of magma layers in the overall mushy system as described in Cashman *et al*. (2017). Mushy systems containing low-density, melt-rich lenses will be inherently gravitationally unstable, and this could drive destabilisation. Finally, a tectonic trigger cannot be ruled out.

Since the caldera of the ignimbrite is unidentified, we can only provide a very rough estimate for the areal footprint of the Cardones ignimbrite. The outflow volume has a volume of at least 1260 km^3 (García *et al*. 2004) and the total erupted volume is likely two or three times greater if intercaldera ignimbrite fill and co-ignimbrite ash are included. If we use the depth range of 6 to 9 ± 2 km for a crust with density 2600 kg/m^3 and suggest 2000 to 3000 km^3 of magma was erupted, we calculate an areal

footprint on the order of 1000 km^2, comparable in size to other known calderas associated with similar sized eruptions (e.g. Folkes *et al*., 2011; Chesner & Rose, 1991).

CONCLUDING STATEMENT

Our vision for the evolution of the Cardones magma system is the emplacement of a large batholith-scale silicic magmatic system over a period on the order of 200 kyrs. The rhyodacitic magmas were generated by fractional crystallisation from wet mafic to intermediate magmas in the deeper crust, which is represented as antecrystal remnants in rhyodacitic pumice clasts. The shallow magmatic system developed at ~200 MPa through episodic supply of magma. Informed by thermal modelling (e.g. Annen, 2009), we suggest that the system developed into multiple magma layers embedded into likely large volumes of mush over a significant depth range. We found evidence for at least two, petrologically distinct magmas (sandine-poor and sanidine-rich magma), which had variable pre-eruptive temperatures and melt compositions. These multiple magma batches may have developed by melt segregation from a consolidating mush as well as replenishment and amalgamation of segregated melt-rich layers. A major destabilisation event resulted in catastrophic amalgamation of different magmas and crystal mush to form a very large eruptible magma body.

ACKNOWLEDGEMENTS

This project was funded by BHP Billiton. Funding of LA-ICP-MS zircon analyses was provided by Natural Environment Research Council Isotope Geosciences Facilities Steering Committee [grant number IP-1466-1114]. Analytical work would not have been possible without technical support from Nick Roberts, Simon Tapster,

Simon Chenery. SEM-imagery and EMPA-analyses were gathered with support of Stuart Kearns and Ben Buse. The manuscript has benefitted from constructive reviews by Amy Gilmer, Kathy Cashman, Tim Druitt, Ben Ellis, Anita Grunder, an anonymous reviewer and editor Gerhard Wörner.

REFERENCES

Almeev, R. R., Bolte, T., Nash, B. P., Holtz, F., Erdmann, M. & Cathey, H. E. (2012). High-temperature, low-H2O silicic magmas of the Yellowstone hotspot: an experimental study of rhyolite from the Bruneau–Jarbidge Eruptive Center, Central Snake River Plain, USA. *Journal of Petrology* **53**, 1837-1866.

Annen, C. (2009). From plutons to magma chambers: thermal constraints on the accumulation of eruptible silicic magma in the upper crust. *Earth and Planetary Science Letters* **284**, 409-416.

Annen, C., Blundy, J. & Sparks, R. (2006). The genesis of intermediate and silicic magmas in deep crustal hot zones. *Journal of Petrology* **47**, 505-539.

Annen, C., Blundy, J. D., Leuthold, J. & Sparks, R. S. J. (2015). Construction and evolution of igneous bodies: Towards an integrated perspective of crustal magmatism. *Lithos* **230**, 206-221.

Bachmann, O. & Bergantz, G. W. (2004). On the origin of crystal-poor rhyolites: extracted from batholithic crystal mushes. *Journal of Petrology* **45**, 1565-1582.

Bachmann, O. & Bergantz, G. W. (2006). Gas percolation in upper-crustal silicic crystal mushes as a mechanism for upward heat advection and rejuvenation of near-solidus magma bodies. *Journal of Volcanology and Geothermal Research* **149**, 85-102.

Bachmann, O. & Bergantz, G. W. (2008). Rhyolites and their source mushes across tectonic settings. *Journal of Petrology* **49**, 2277-2285.

Bachmann, O., Deering, C. D., Lipman, P. W. & Plummer, C. (2014). Building zoned ignimbrites by recycling silicic cumulates: insight from the 1,000 km3 Carpenter Ridge Tuff, CO. *Contributions to Mineralogy and Petrology* **167**, 1-13.

Bachmann, O. & Dungan, M. A. (2002). Temperature-induced Al-zoning in hornblendes of the Fish Canyon magma, Colorado. *American Mineralogist* **87**, 1062-1076.

Bachmann, O., Dungan, M. A. & Lipman, P. W. (2002). The Fish Canyon magma body, San Juan volcanic field, Colorado: rejuvenation and eruption of an upper-crustal batholith. *Journal of Petrology* **43**, 1469-1503.

Blatter, D. L., Sisson, T. W. & Hankins, W. B. (2017). Voluminous arc dacites as amphibole reaction-boundary liquids. *Contributions to Mineralogy and Petrology* **172**, 27.

Blum‐Oeste, M. & Wörner, G. (2016). Central Andean magmatism can be constrained by three ubiquitous end‐members. *Terra Nova* **28**, 434-440.

Blundy, J. & Cashman, K. (2001). Ascent-driven crystallisation of dacite magmas at Mount St Helens, 1980-1986. *Contributions to Mineralogy and Petrology* **140**, 631-650.

Blundy, J., Cashman, K. V. & Berlo, K. (2008). Evolving magma storage conditions beneath Mount St. Helens inferred from chemical variations in melt inclusions from the 1980–1986 and current (2004–2006) eruptions. A volcano rekindled: the renewed eruption of Mount St. Helens 2006, Edited by David R. Sherrod, William E. Scott, and Peter H. Stauffer, *U.S. Geological Survey Professional Paper* **755-790**.

Blundy, J., Cashman, K. & Humphreys, M. (2006). Magma heating by decompression-driven crystallization beneath andesite volcanoes. *Nature* **443**, 76-80.

Blundy, J. D. & Holland, T. J. (1990). Calcic amphibole equilibria and a new amphibole-plagioclase geothermometer. *Contributions to mineralogy and petrology* **104**, 208-224.

Blundy, J. D. & Shimizu, N. (1991). Trace element evidence for plagioclase recycling in calc-alkaline magmas. *Earth and Planetary Science Letters* **102**, 178-197.

Blundy, J. D. & Wood, B. J. (1991). Crystal-chemical controls on the partitioning of Sr and Ba between plagioclase feldspar, silicate melts, and hydrothermal solutions. *Geochimica et Cosmochimica Acta* **55**, 193-209.

Boehnke, P., Watson, E. B., Trail, D., Harrison, T. M. & Schmitt, A. K. (2013). Zircon saturation re-revisited. Chemical Geology 351, 324-334.

Bolte, T., Holtz, F., Almeev, R. & Nash, B. (2015). The Blacktail Creek Tuff: an analytical and experimental study of rhyolites from the Heise volcanic field, Yellowstone hotspot system. *Contributions to Mineralogy and Petrology* **169**, 1-24.

Brandmeier, M. & Wörner, G. (2016). Compositional variations of ignimbrite magmas in the Central Andes over the past 26Ma—A multivariate statistical perspective. Lithos 262, 713-728.

Burgisser, A. & Bergantz, G. W. (2011). A rapid mechanism to remobilize and homogenize highly crystalline magma bodies. *Nature* **471**, 212-215.

Cadoux, A., Scaillet, B., Druitt, T. H. & Deloule, E. (2014). Magma storage conditions of large Plinian eruptions of Santorini Volcano (Greece). Journal of *Petrology* **55**, 1129-1171.

Chamberlain, K. J., Wilson, C. J. N., Wooden, J. L., Charlier, B. L. A., & Ireland, T. R. (2013). New perspectives on the Bishop Tuff from zircon textures, ages and trace elements. *Journal of Petrology*, egt072.

Caricchi, L. & Blundy, J. (2015). Experimental petrology of monotonous intermediate magmas. *Geological Society, London, Special Publications* **422**, 105-130.

Cashman, K. & Blundy, J. (2013). Petrological cannibalism: the chemical and textural consequences of incremental magma body growth. *Contributions to Mineralogy and Petrology* **166**, 703-729.

Cashman, K. V. & Giordano, G. (2014). Calderas and magma reservoirs. *Journal of Volcanology and Geothermal Research* **288**, 28-45.

Cashman K.V., Sparks, R.S.J. and Blundy J. (2017). Vertically extensive and unstable crystals mushes: a unifying view of igneous processes associated with volcanoes. *Science* **355** eaag3055.

Chesner, C. A. (1998). Petrogenesis of the toba tuffs, sumatra, indonesia. *Journal of Petrology* **39**, 397-438.

Chesner, C. A. & Rose, W. I. (1991). Stratigraphy of the Toba tuffs and the evolution of the Toba caldera complex, Sumatra, Indonesia. *Bulletin of Volcanology* **53**, 343-356.

Chmielowski, J., Zandt, G. & Haberland, C. (1999). The central Andean Altiplano - Puna magma body. *Geophysical Research Letters* **26**, 783-786.

Claiborne, L. L., Miller, C., Walker, B., Wooden, J., Mazdab, F. & Bea, F. (2006). Tracking magmatic processes through Zr/Hf ratios in rocks and Hf and Ti zoning in zircons: an example from the Spirit Mountain batholith, Nevada. *Mineralogical Magazine* **70**, 517-543.

Claiborne, L. L., Miller, C. F. & Wooden, J. L. (2010). Trace element composition of igneous zircon: a thermal and compositional record of the accumulation and evolution of a large silicic batholith, Spirit Mountain, Nevada. *Contributions to Mineralogy and Petrology* **160**, 511-531.

Cooper, G. F. & Wilson, C. J. (2014). Development, mobilisation and eruption of a large crystal-rich rhyolite: the Ongatiti ignimbrite, New Zealand. *Lithos* **198**, 38-57.

Cooper, G. F., Wilson, C. J., Charlier, B. L., Wooden, J. L. & Ireland, T. R. (2014). Temporal evolution and compositional signatures of two supervolcanic systems recorded in zircons from Mangakino volcanic centre, New Zealand. *Contributions to Mineralogy and Petrology* **167**, 1-23.

Cooper, G. F., Wilson, C. J., Millet, M.-A., Baker, J. A. & Smith, E. G. (2012). Systematic tapping of independent magma chambers during the 1Ma Kidnappers supereruption. *Earth and Planetary Science Letters* **313**, 23-33.

Couch, S., Sparks, R.S.J. & Carroll, M.R. (2001). Mineral disequilibrium in lavas explained by convective self-mixing in open magma chambers. *Nature* **411**, 1037-1039.

Davidson, J., Turner, S., Handley, H., Macpherson, C. & Dosseto, A. (2007). Amphibole “sponge” in arc crust? *Geology* **35**, 787-790.

De Silva, S. (1989). Altiplano-Puna volcanic complex of the central Andes. *Geology* **17**, 1102-1106.

De Silva, S. & Gosnold, W. (2007). Episodic construction of batholiths: insights from the spatiotemporal development of an ignimbrite flare-up. *Journal of Volcanology and Geothermal Research* **167**, 320 –335.

de Silva, S., Salas, G. & Schubring, S. (2008). Triggering explosive eruptions—The case for silicic magma recharge at Huaynaputina, southern Peru. *Geology* **36**, 387-390.

De Silva, S., Zandt, G., Trumbull, R., Viramonte, J. G., Salas, G. & Jiménez, N. (2006). Large ignimbrite eruptions and volcano-tectonic depressions in the Central Andes: a thermomechanical perspective. *Geological Society, London, Special Publications* **269**, 47-63.

Druitt, T. H., Costa, F., Deloule, E., Dungan, M. & Scaillet, B. (2012). Decadal to monthly timescales of magma transfer and reservoir growth at a caldera volcano. *Nature* **482**, 77-80.

Eddy, M. P., Bowring, S. A., Miller, R. B. & Tepper, J. H. (2016). Rapid assembly and crystallization of a fossil large-volume silicic magma chamber. *Geology*, G37631. 37631.

Elkins, L. T. & Grove, T. L. (1990). Ternary feldspar experiments and thermodynamic models. *American Mineralogist* **75**, 544-559.

Ellis, B. S. & Wolff, J. A. (2012). Complex storage of rhyolite in the central Snake River Plain. *Journal of Volcanology and Geothermal Research* **211**, 1-11.

Ellis, B. S., Bachmann, O. & Wolff, J. A. (2014). Cumulate fragments in silicic ignimbrites: The case of the Snake River Plain. *Geology* **42**, 431-434.

Ewart, A. & Griffin, W. (1994). Application of proton-microprobe data to trace-element partitioning in volcanic rocks. *Chemical Geology* **117**, 251-284.

Ferry, J. & Watson, E. (2007). New thermodynamic models and revised calibrations for the Ti-in-zircon and Zr-in-rutile thermometers. *Contributions to Mineralogy and Petrology* **154**, 429-437.

Folkes, C. B., Wright, H. M., Cas, R. A., de Silva, S. L., Lesti, C. & Viramonte, J. G. (2011). A re-appraisal of the stratigraphy and volcanology of the Cerro Galán volcanic system, NW Argentina. *Bulletin of volcanology* **73**, 1427-1454.

Frazer, R. E., Coleman, D. S. & Mills, R. D. (2014). Zircon U-Pb geochronology of the Mount Givens Granodiorite: Implications for the genesis of large volumes of eruptible magma. *Journal of Geophysical Research: Solid Earth* **119**, 2907-2924.

Freymuth, H., Brandmeier, M. & Wörner, G. (2015). The origin and crust/mantle mass balance of Central Andean ignimbrite magmatism constrained by oxygen and strontium isotopes and erupted volumes. *Contributions to Mineralogy and Petrology* **169**, 1-24.

Fuhrman, M. L. & Lindsley, D. H. (1988). Ternary-feldspar modeling and thermometry. *American Mineralogist* **73**, 201-215.

García, M., Gardeweg, M., Clavero, J. & Hérail, G. (2004). Arica map: Tarapacá Region, scale 1: 250,000. *Serv. Nac. Geol. Min* **84**, 150.

Ghiorso, M. S. (1984). Activity/composition relations in the ternary feldspars. *Contributions to Mineralogy and Petrology* **87**, 282-296.

Ginibre, C., Wörner, G. & Kronz, A. (2004). Structure and dynamics of the Laacher See magma chamber (Eifel, Germany) from major and trace element zoning in sanidine: a cathodoluminescence and electron microprobe study. *Journal of Petrology* **45**, 2197-2223.

Glazner, A. F., Bartley, J. M., Coleman, D. S., Gray, W. & Taylor, R. Z. (2004). Are plutons assembled over millions of years by amalgamation from small magma chambers? *GSA today* **14**, 4-12.

Green, N. L. & Usdansky, S. I. (1986). Ternary-feldspar mixing relations and thermobarometry. *American Mineralogist* **71**, 1100-1108.

Gualda, G. A. & Ghiorso, M. S. (2013). The Bishop Tuff giant magma body: an alternative to the Standard Model. *Contributions to Mineralogy and Petrology* **166**, 755-775.

Hasofer, A. (1963). On the reliability of the point-counter method in petrography. *Aust. J. Appl. Sci* **14**, 168-179.

Hayden, L. A. & Watson, E. B. (2007). Rutile saturation in hydrous siliceous melts and its bearing on Ti-thermometry of quartz and zircon. *Earth and Planetary Science Letters* **258**, 561-568.

Herrmann, W. & Berry, R. F. (2002). MINSQ–a least squares spreadsheet method for calculating mineral proportions from whole rock major element analyses. *Geochemistry: Exploration, Environment, Analysis* **2**, 361-368.

Hildreth, W. (1979). The Bishop Tuff: evidence for the origin of compositional zonation in silicic magma chambers. *Geological Society of America Special Papers* **180**, 43-76.

Hildreth, W. (1981). Gradients in silicic magma chambers: implications for lithospheric magmatism. *Journal of Geophysical Research: Solid Earth (1978–2012)* **86**, 10153-10192.

Hildreth, W. (2004). Volcanological perspectives on Long Valley, Mammoth Mountain, and Mono Craters: several contiguous but discrete systems. *Journal of Volcanology and Geothermal Research* **136**, 169-198.

Hoke, L. & Lamb, S. (2007). Cenozoic behind-arc volcanism in the Bolivian Andes, South America: implications for mantle melt generation and lithospheric structure. *Journal of the Geological Society* **164**, 795-814.

Holland, T. & Blundy, J. (1994). Non-ideal interactions in calcic amphiboles and their bearing on amphibole-plagioclase thermometry. *Contributions to Mineralogy and Petrology* **116**, 433-447.

Hoskin, P. W. & Schaltegger, U. (2003). The composition of zircon and igneous and metamorphic petrogenesis. *Reviews in mineralogy and geochemistry* **53**, 27-62.

Huber, C., Bachmann, O. & Dufek, J. (2012). Crystal-poor versus crystal-rich ignimbrites: A competition between stirring and reactivation. *Geology* **40**, 115-118.

Huppert, H. E. & Sparks, R. S. J. (1988). The generation of granitic magmas by intrusion of basalt into continental crust. *Journal of Petrology* **29**, 599-624.

Jackson, M. D., Cheadle, M. J. & Atherton, M. P. (2003). Quantitative modeling of granitic melt generation and segregation in the continental crust. *Journal of Geophysical Research: Solid Earth* **108**.

James, D. E. (1971). Plate tectonic model for the evolution of the Central Andes. *Geological Society of America Bulletin* **82**, 3325-3346.

Johannes, W. Holtz, F. (1996) *Petrogenesis and Experimental Petrology of Granitic Rocks*. Springer-Verlag, Berlin.

Johnson, M. C. & Rutherford, M. J. (1989). Experimental calibration of the aluminum-in-hornblende geobarometer with application to Long Valley caldera (California) volcanic rocks. *Geology* **17**, 837-841.

Kay, S. M. & Coira, B. L. (2009). Shallowing and steepening subduction zones, continental lithospheric loss, magmatism, and crustal flow under the Central Andean Altiplano-Puna Plateau. *Geological Society of America Memoirs* **204**, 229-259.

Kay, S. M., Coira, B. L., Caffe, P. J. & Chen, C.-H. (2010). Regional chemical diversity, crustal and mantle sources and evolution of central Andean Puna plateau ignimbrites. *Journal of Volcanology and Geothermal Research* **198**, 81-111.

Klimm, K., Holtz, F., Johannes, W. & King, P. (2003). Fractionation of metaluminous A-type granites: an experimental study of the Wangrah Suite, Lachlan Fold Belt, Australia. *Precambrian Research* **124**, 327-341.

Lahsen, A. (1982). Upper Cenozoic volcanism and tectonism in the Andes of northern Chile. *Earth-Science Reviews* **18**, 285-302.

Laumonier, M., Gaillard, F., Muir, D., Blundy, J., Unsworth, M. 2017. A giant magmatic water reservoir in the Altiplano-Puna crust. *Earth and Planetary Science Letters* **457**, 173-180 doi: 10.1016/j.epsl.2016.10.023

Leake, B., Hawthorne, F. C., Kato, A., Kisch, H. J., Krivovichev, V. G., Linthout, K., Laird, J., Maresch, W. V., Schumacher, J. C., Stephenson, N. C. & Whittaker, E. J. (1997). Nomenclature of amphiboles: report of the subcommittee on amphiboles of the International Mineralogical Association, Commission on New Minerals and Mineral Names. *Can Mineral* **35**, 219246.

Lindsay, J., Schmitt, A., Trumbull, R., De Silva, S., Siebel, W. & Emmermann, R. (2001). Magmatic evolution of the La Pacana caldera system, Central Andes, Chile: compositional variation of two cogenetic, large-volume felsic ignimbrites. *Journal of Petrology* **42**, 459-486.

Lindsley, D. & Nekvasil, H. (1989). A ternary feldspar model for all reasons. *Eos* **70**, 506.

Lipman, P. W. & Bachmann, O. (2015). Ignimbrites to batholiths: Integrating perspectives from geological, geophysical, and geochronological data. *Geosphere*, GES01091. 01091.

Lipman, P., Dungan, M. & Bachmann, O. (1997). Comagmatic granophyric granite in the Fish Canyon Tuff, Colorado: implications for magma-chamber processes during a large ash-flow eruption. *Geology* **25**, 915-918.

Lord, G. & Willis, T. (1951). Calculation of air bubble size distribution from results of a Rosiwal traverse of aerated concrete. *ASTM Bulletin* **177**, 56.

Lukács, R., Harangi, S., Bachmann, O., Guillong, M., Danišík, M., Buret, Y., von Quadt, A., Dunkl, I., Fodor, L. & Sliwinski, J. (2015). Zircon geochronology and geochemistry to constrain the youngest eruption events and magma evolution of the Mid-Miocene ignimbrite flare-up in the Pannonian Basin, eastern central Europe. *Contributions to Mineralogy and Petrology* **170**, 1-26.

Mamani, M., Wörner, G. & Sempere, T. (2010). Geochemical variations in igneous rocks of the Central Andean orocline (13 S to 18 S): Tracing crustal thickening and magma generation through time and space. *Geological Society of America Bulletin* **122**, 162-182.

Mason, B. G., Pyle, D. M. & Oppenheimer, C. (2004). The size and frequency of the largest explosive eruptions on Earth. *Bulletin of Volcanology* **66**, 735-748.

Matzel, J. E., Bowring, S. A. & Miller, R. B. (2006). Time scales of pluton construction at differing crustal levels: Examples from the Mount Stuart and Tenpeak intrusions, North Cascades, Washington. *Geological Society of America Bulletin* **118**, 1412-1430.

Maughan, L. L., Christiansen, E. H., Best, M. G., Gromme, C. S., Deino, A. L. & Tingey, D. G. (2002). The Oligocene Lund Tuff, Great Basin, USA: a very large volume monotonous intermediate. *Journal of Volcanology and Geothermal Research* **113**, 129-157.

Miller, C. F., McDowell, S. M. & Mapes, R. W. (2003). Hot and cold granites? Implications of zircon saturation temperatures and preservation of inheritance. *Geology* **31**, 529-532.

Muir, D. D., Blundy, J. D., Hutchinson, M. C. & Rust, A. C. (2014). Petrological imaging of an active pluton beneath Cerro Uturuncu, Bolivia. *Contributions to Mineralogy and Petrology* **167,** 1-25.

Mutch, E., Blundy, J., Tattitch, B., Cooper, F. & Brooker, R. (2016). An experimental study of amphibole stability in low-pressure granitic magmas and a revised Al-in-hornblende geobarometer. *Contributions to Mineralogy and Petrology* **171**, 85.

Naney, M. (1983). Phase equilibria of rock-forming ferromagnesian silicates in granitic systems. *American journal of science* **283**, 993-1033.

Nekvasil, H. & Burnham, C. W. (1987). The calculated individual effects of pressure and water content on phase equilibria in the granite system. *Magmatic processes: physicochemical principles*: The Geochemical Society, Lancaster Press Lancaster, 433-445.

Perkins, J.P., Ward, K.M., de Silva, S., Zandt,G., Beck, S.L. & Finnegan, N.J. (2016). Surface uplift in the Central Andes driven by growth of the Altiplano Puna Magma Body. *Nature Communications* **7**, 13185.

Prouteau, G. & Scaillet, B. (2003). Experimental constraints on the origin of the 1991 Pinatubo dacite. *Journal of Petrology* **44**, 2203-2241.

Putirka, K. D. (2008). Thermometers and barometers for volcanic systems. *Reviews in Mineralogy and Geochemistry* **69**, 61-120.

Reid, M. R. (2008). How long does it take to supersize an eruption? *Elements* **4**, 23-28.

Reid, M. R. & Vazquez, J. A. (2016). Fitful and protracted magma assembly leading to a Giant eruption, Youngest Toba Tuff, Indonesia. Geochemistry, Geophysics, Geosystems.

Ren, M. (2004). Partitioning of Sr, Ba, Rb, Y, and LREE between alkali feldspar and peraluminous silicic magma. *American Mineralogist* **89**, 1290-1303.

Riker, J. M., Blundy, J. D., Rust, A. C., Botcharnikov, R. E. & Humphreys, M. C. (2015). Experimental phase equilibria of a Mount St. Helens rhyodacite: a framework for interpreting crystallization paths in degassing silicic magmas. *Contributions to Mineralogy and Petrology* **170**, 1-22.

Roduit, N. (2008). JMicroVision: Image analysis toolbox for measuring and quantifying components of high-definition images. Version 1.2. 7. Software available for free download at http://www. jmicrovision. com.

Salisbury, M. J., Jicha, B. R., de Silva, S. L., Singer, B. S., Jiménez, N. C. & Ort, M. H. (2010). 40Ar/39Ar chronostratigraphy of Altiplano-Puna volcanic complex ignimbrites reveals the development of a major magmatic province. *Geological Society of America Bulletin*, B30280. 30281.

Scaillet, B. & Evans, B. W. (1999). The 15 June 1991 eruption of Mount Pinatubo. I. Phase equilibria and pre-eruption P–T–fO2–fH2O conditions of the dacite magma. *Journal of Petrology* **40**, 381-411.

Scaillet, B., Pichavant, M. & Roux, J. (1995). Experimental crystallization of leucogranite magmas. *Journal of Petrology* **36**, 663-705.

Schmidt, M. W. (1992). Amphibole composition in tonalite as a function of pressure: an experimental calibration of the Al-in-hornblende barometer. Contributions to mineralogy and petrology **110**, 304-310.

Schoene, B., Schaltegger, U., Brack, P., Latkoczy, C., Stracke, A. & Günther, D. (2012). Rates of magma differentiation and emplacement in a ballooning pluton recorded by U–Pb TIMS-TEA, Adamello batholith, Italy. *Earth and Planetary Science Letters* **355**, 162-173.

Smith, R. L. (1979). Ash-flow magmatism. *Geological Society of America Special Papers* **180**, 5-28.

Smith, D. J. (2014). Clinopyroxene precursors to amphibole sponge in arc crust. *Nature communications* **5**.

Smith, R. L. & Bailey, R. A. (1966). The Bandelier Tuff: a study of ash-flow eruption cycles from zoned magma chambers. *Bulletin of Volcanology* **29**, 83-103.

Solano, J., Jackson, M., Sparks, R., Blundy, J. & Annen, C. (2012). Melt segregation in deep crustal hot zones: a mechanism for chemical differentiation, crustal assimilation and the formation of evolved magmas. *Journal of Petrology*, egs041.

Streck, M. J. (2008). Mineral textures and zoning as evidence for open system processes. *Reviews in Mineralogy and Geochemistry* **69**, 595-622.

Sun, S.-S. & McDonough, W.-s. (1989). Chemical and isotopic systematics of oceanic basalts: implications for mantle composition and processes. Geological Society, London, Special Publications 42, 313-345.

Tattitch, B., Blundy, J., 2017. Cu-Mo partitioning between felsic melts and saline-aqueous fluids as a function of $X_{NaCl(eq)}$, fO_2 and fS_2. American Mineralogist doi. 10.2138/am-2017-5998

Tsuchiyama, A. (1985). Dissolution kinetics of plagioclase in the melt of the system diopside-albite-anorthite, and origin of dusty plagioclase in andesites. *Contributions to Mineralogy and Petrology* **89**, 1-16.

Tindle, A. G. & Pearce, J. A. (1981). Petrogenetic modelling of in situ fractional crystallization in the zoned Loch Doon Pluton, Scotland. *Contributions to Mineralogy and Petrology* **78**, 196-207.

Tuttle, O. F. & Bowen, N. L. (1958). Origin of granite in the light of experimental studies in the system NaAlSi3O8–KAlSi3O8–SiO2–H2O. *Geological Society of America Memoirs* **74**, 1-146.

van Zalinge, M., Sparks, R., Cooper, F. & Condon, D. (2016). Early Miocene large-volume ignimbrites of the Oxaya Formation, Central Andes. *Journal of the Geological Society*, jgs2015-2123.

Walker, B. A., Klemetti, E. W., Grunder, A. L., Dilles, J. H., Tepley, F. J. & Giles, D. (2013). Crystal reaming during the assembly, maturation, and waning of an eleven-million-year crustal magma cycle: thermobarometry of the Aucanquilcha Volcanic Cluster. *Contributions to Mineralogy and Petrology* **165**, 663-682.

Ward, K. M., Zandt, G., Beck, S. L., Christensen, D. H. & McFarlin, H. (2014). Seismic imaging of the magmatic underpinnings beneath the Altiplano-Puna volcanic complex from the joint inversion of surface wave dispersion and receiver functions. *Earth and Planetary Science Letters* **404**, 43-53.

Watson, E. & Harrison, T. (2005). Zircon thermometer reveals minimum melting conditions on earliest Earth. *Science* **308**, 841-844.

Watson, E., Wark, D. & Thomas, J. (2006). Crystallization thermometers for zircon and rutile. *Contributions to Mineralogy and Petrology* **151**, 413-433.

Watson, E. B. & Harrison, T. M. (1983). Zircon saturation revisited: temperature and composition effects in a variety of crustal magma types. *Earth and Planetary Science Letters* **64**, 295-304.

Watts, K. E., John, D. A., Colgan, J. P., Henry, C. D., Bindeman, I. N. & Schmitt, A. K. (2016). Probing the Volcanic–Plutonic Connection and the Genesis of Crystal-rich Rhyolite in a Deeply Dissected Supervolcano in the Nevada Great Basin: Source of the Late Eocene Caetano Tuff. *Journal of Petrology* **57**, 1599-1644.

Wen, S. & Nekvasil, H. (1994). SOLVALC: An interactive graphics program package for calculating the ternary feldspar solvus and for two-feldspar geothermometry. *Computers & Geosciences* **20**, 1025-1040.

Willcock, M., Bargossi, G., Weinberg, R., Gasparotto, G., Cas, R., Giordano, G. & Marocchi, M. (2015). A complex magma reservoir system for a large volume intra-to extra-caldera ignimbrite: Mineralogical and chemical architecture of the VEI8, Permian Ora ignimbrite (Italy). *Journal of Volcanology and Geothermal Research* **306**, 17-40.

Wolff, J., Ellis, B., Ramos, F., Starkel, W., Boroughs, S., Olin, P. & Bachmann, O. (2015). Remelting of cumulates as a process for producing chemical zoning in silicic tuffs: A comparison of cool, wet and hot, dry rhyolitic magma systems. *Lithos* **236**, 275-286.

Wotzlaw, J.-F., Bindeman, I. N., Stern, R. A., D'Abzac, F.-X. & Schaltegger, U. (2015). Rapid heterogeneous assembly of multiple magma reservoirs prior to Yellowstone supereruptions. *Scientific reports* **5**.

Wotzlaw, J.-F., Schaltegger, U., Frick, D. A., Dungan, M. A., Gerdes, A. & Günther, D. (2013). Tracking the evolution of large-volume silicic magma reservoirs from assembly to supereruption. *Geology* **41**, 867-870.

Wright, H. M., Folkes, C. B., Cas, R. A. & Cashman, K. V. (2011). Heterogeneous pumice populations in the 2.08-Ma Cerro Galán Ignimbrite: implications for magma recharge and ascent preceding a large-volume silicic eruption. *Bulletin of volcanology* **73**, 1513-1533.

Wörner, G., Hammerschmidt, K., Henjes-Kunst, F., Lezaun, J. & Wilke, H. (2000). Geochronology (40Ar/39Ar, K-Ar and He-exposure ages) of Cenozoic magmatic rocks from Northern Chile (18-22° S): implications for magmatism and tectonic evolution of the central Andes. *Revista geológica de Chile* **27**, 205-240.

Zandt, G., Leidig, M., Chmielowski, J., Baumont, D. & Yuan, X. (2003). Seismic detection and characterization of the Altiplano-Puna magma body, central Andes. *Pure and Applied Geophysics* **160**, 789-807.

Zellmer, G. F. & Clavero, J. E. (2006). Using trace element correlation patterns to decipher a sanidine crystal growth chronology: an example from Taapaca volcano, Central Andes. *Journal of Volcanology and Geothermal Research* **156**, 291-301.

Figure Captions

Fig. 1. Digital elevation model (DEM) of the Western Andean Slope in northern Chile. (b) Geological map of study area (modified after García *et al*., 2004) with the drill hole locations and the Molinos section. (c) Stratigraphy of the Cardones ignimbrite (modified after van Zalinge *et al*., 2016) with sample locations.

Fig. 2. Photographs of wetted drill core showing: (a) a crystal-rich pumice clast (CRP) flattened into a fiamma. The large visible euhedral crystals are feldspars and quartz; (b) a crystal-poor pumice clast (CPP) that is red in color and intensely flattened into a fiamma; (c) a slightly flattened microdioritic enclave that is dark in color. Large white crystals are entrained from rhyolitic magma and give an inhomogeneous texture to the enclave; (d) a dacitic enclave with plastic deformation along the margins, suggesting the enclave was hot when entrained. Arrows point in the upward direction of the drill core. Grey-scale of BSE-images of: (e) CRP and (f) CPP.

Fig. 3. a) Qtz-Plag-San ternary diagram of crystal modes from pumice and bulk rock from the Cardones ignimbrite. Note that about half of the pumice clasts is sanidine-poor, whereas the other half contains significantly more sanidine. b) Vertical distribution of pumice clasts in Unit 1. Note that both sanidine-poor and sanidine-rich pumice clasts are found throughout its entire thickness. (Pumice clast data are compilation of this study and van Zalinge *et al*. (2016) (full data set in Supplementary Data Table 2); bulk rock data are from van Zalinge *et al.* (2016))

Fig. 4. Major element variation diagrams for pumice clasts, enclaves and bulk rocks from Unit 1. The pumice analyses indicated with a '*' are corrected for secondary calcite content. Where possible pumice is categorized as sanidine-poor or sanidine rich. In the SiO_2 – K_2O diagram two trends can be identified. (Data originally

presented in van Zalinge *et al*., 2016)

Fig. 5. Trace element variation diagrams for Unit 1 showing: (a) Sr against SiO_2 and (b) Ba against SiO_2. All pumice with obvious secondary calcite alteration excluded. The average composition for sanidine-poor and sanidine-rich pumice clasts and fractionation results are plotted in terms of (c) Sr against Rb; and (d) Sr against Ba. The solid black arrows present results of Rayleigh fractionation modelling and the dotted arrows show results for equilibrium crystallisation modelling, with the tics indicating percentages of crystallisation in steps of 10. See text in 'Discussion' for further explanation. Trace-element data from van Zalinge *et al*. (2016).

Fig. 6. Normative compositions for major components of Unit 1 plotted on: (a) Qtz-Ab-Or ternary diagram with cotectic minima for a water-saturated haplogranitic system at various pressures (diagram modified from Blundy & Cashman, 2001); (b) Qtz-Ab-Or ternary diagram with isotherms for a water-saturated haplogranititc system at 200 MPa (diagram modified from Tuttle & Bowen, 1958).

Fig. 7. Representative grey-scale BSE-images of plagioclase in: (a)-(b) sanidine-poor pumice; (c)-(d) sanidine-rich pumice. The An-content along the profile indicated in the images is plotted below each image.

Fig. 8. An-content versus Ba diagrams for: (a) plagioclase phenocrysts from sanidine-poor pumices; (b) plagioclase phenocrysts from sanidine-rich pumices; (c) plagioclase phenocrysts and microlites in the daticic enclave and microdiorites, respectively; (d) plagioclase inclusions in amphibole, biotite and sanidine. 1σ sd for Ba indicated in the right-hand corner of each diagram. Note that the rims of plagioclase in sanidine-poor pumices and the dacitic enclave contain much more Ba than the rims of plagioclase in sanidine-rich pumices.

Fig. 9. (a) – (c) Grey-scale BSE-image of three types of zoned sanidine that are common in the Cardones ignimbrite; the bright zones contain more Ba than the dark zones. The Ba and Sr composition along the marked profile are plotted below each image. (d) Diagram showing the growth history of these three sanidine types.

Fig. 10. (a) Average sanidine composition in the Cardones ignimbrite in holes 1 and 9 (error-bars are 1σ uncertainty). The diagram for hole 1 also presents two-feldspar temperatures (blue hexagons) calculated with the thermometer of Fuhrman and Lindsley (1988).

Fig. 11. (a) BSE-image of a kinked biotite that is partly intergrown with plagioclase. (b)-(c) Compositional diagrams for biotite in different sample types.

Fig. 12. Representative BSE-images of: (a) high-Al_{tot} amphibole with a reaction rim in a dacitic enclave; (b) amphibole with a resorbed high-Al_{tot} core and a low-Al_{tot} rim in a sanidine-poor pumice; (c) amphibole, from bulk rock, with a low-Al_{tot} core and rim containing plagioclase and biotite inclusions. (d) Histogram showing bimodal distribution of the Al_{tot} composition in amphibole. (f)-(g) Compositional data of Cardones amphiboles. (g)-(i) Compositional diagrams showing representative core-rim compositions connected by tie-lines. The grey area shows typical outermost rim compositions.

Fig. 13. (a) Histogram of zircon aspect ratios. (b) Representative CL-images of zircon crystals in the Cardones ignimbrite. (c) Chondrite-normalised REE spider diagrams (Sun & McDonough, 1989). (d)-(h) Compositional diagrams for zircons; uncertainties presented in the left corners. Tie-lines on the trace-element plots indicate representative core-rim trends. Temperatures are plotted along the diagrams g and h for αTiO_2 is 0.6, 0.7 and 0.8, using the Ti-in-zircon thermometer of Ferry & Watson

(2007).

Fig. 14. (a) Plagioclase-amphibole temperatures plotted against Al_{tot} concentration measured in amphibole. (b) Summary of all thermometry results with the grey bar indicating the H_2O-saturated granite solidus at pressures between 200-500 MPa (Johannes & Holtz, 1996). H&B'94 = Holland & Blundy, 1994; B'13 = Boehnke *et al*., 2013; F&W'07 = Ferry & Watson, 2007; F&L'88 = Fuhrman & Lindsley 1988.

Fig. 15. Plot of pressure against Al_{tot} concentration of amphibole from nine experimental studies on starting compositions similar to Cardones ignimbrites. Note the overall, non-linear increase in Al_{tot} with pressure. The grey boxes indicate typical Al_{tot} concentrations of different amphibole groupings in the Cardones ignimbrite.

Fig. 16. a) Crystallisation sequence for the Cardones system with estimates for pressure, temperature and H_2O-content. b) The two types of magma with their main characteristics.

Fig. 17. Conceptual model for the evolution of the Cardones magmatic system. The shallow system was characterised two magma batches with different petrological features, likely embedded in a crystal-rich mush. Antecrystal remnants indicate that the magmas were derived from a deeper crustal hot zone. Prior to eruption, catastrophic destabilisation of the system led to the formation of a large, heterogeneous eruptible magma body.

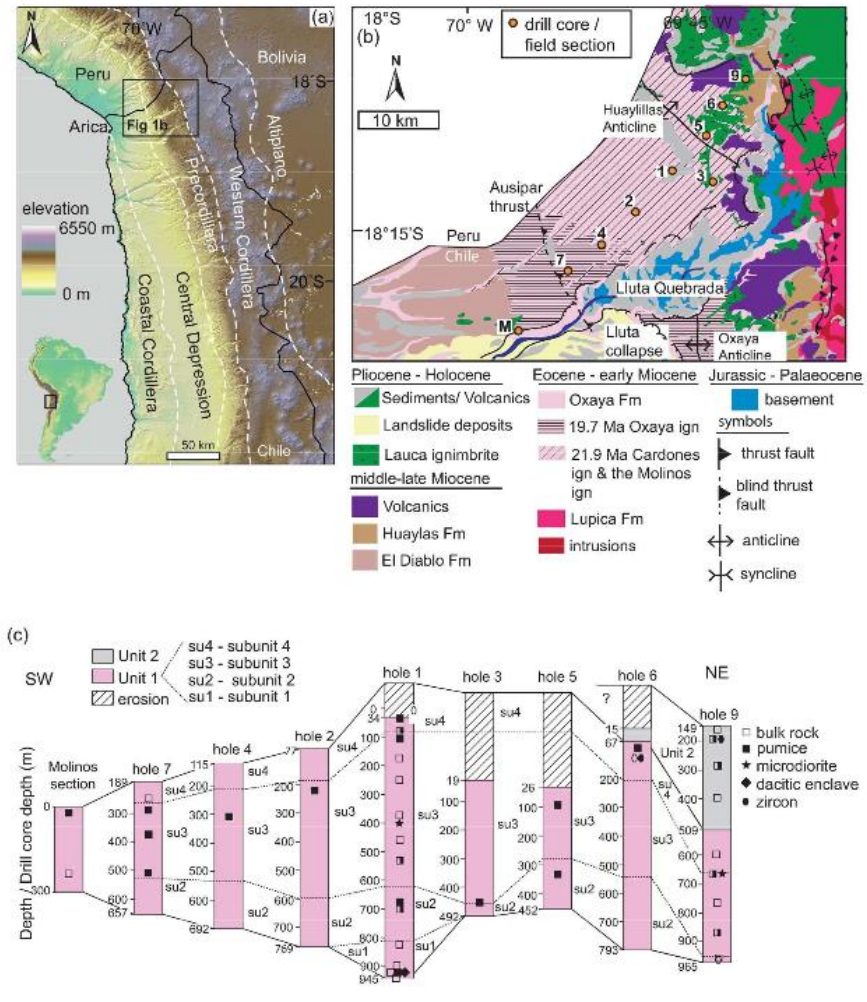

Figure 1. Map and sample locations

247x291mm (300 x 300 DPI)

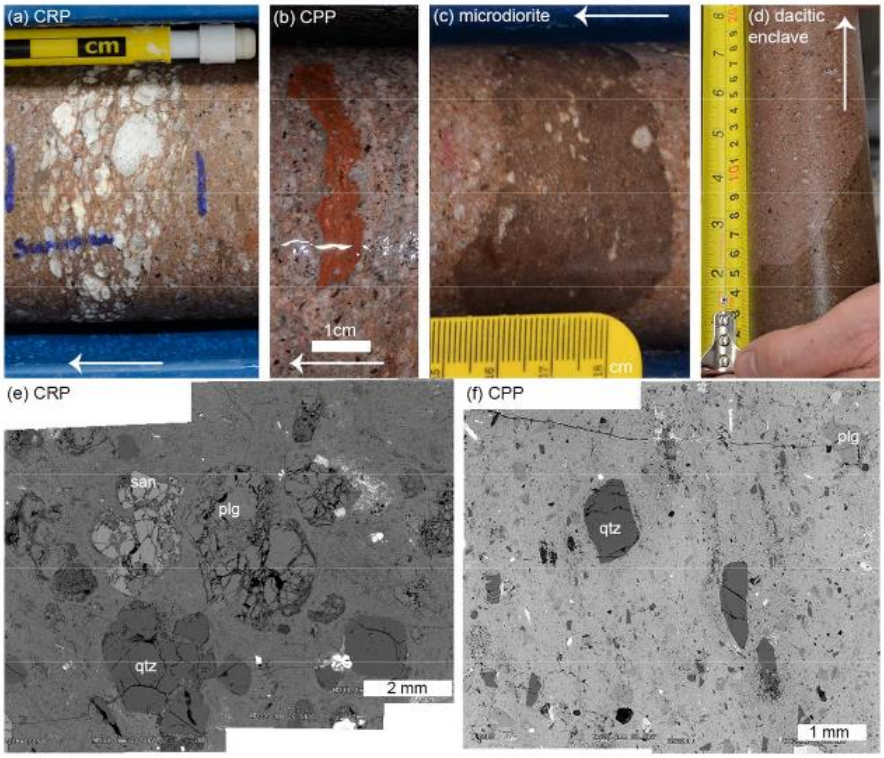

Figure 2. Images of pumice clasts and mafic enclaves

210x179mm (144 x 144 DPI)

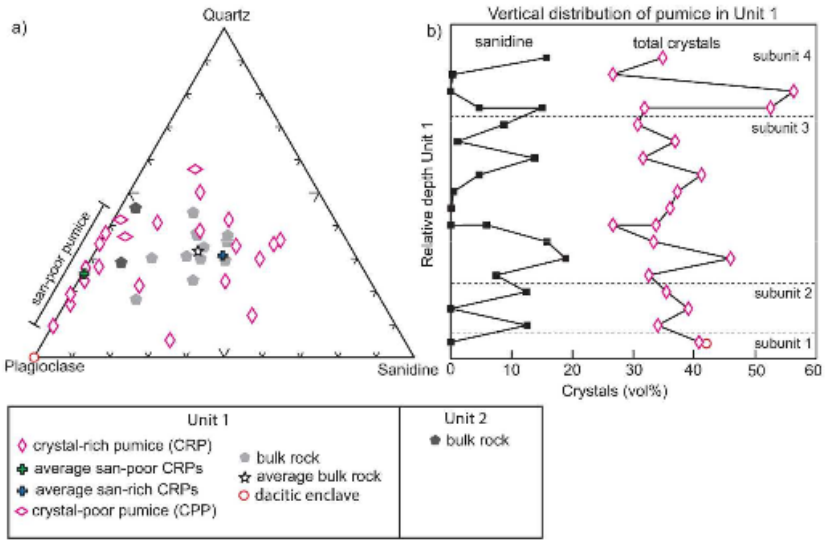

Figure 3. Crystal modes

297x420mm (300 x 300 DPI)

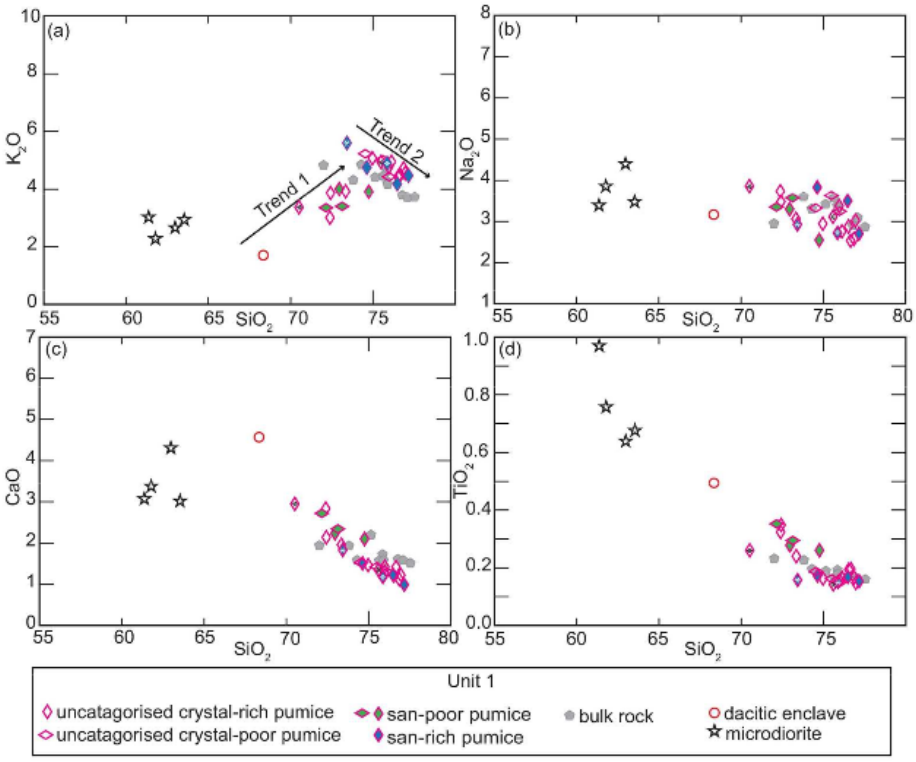

Major elements

174x146mm (300 x 300 DPI)

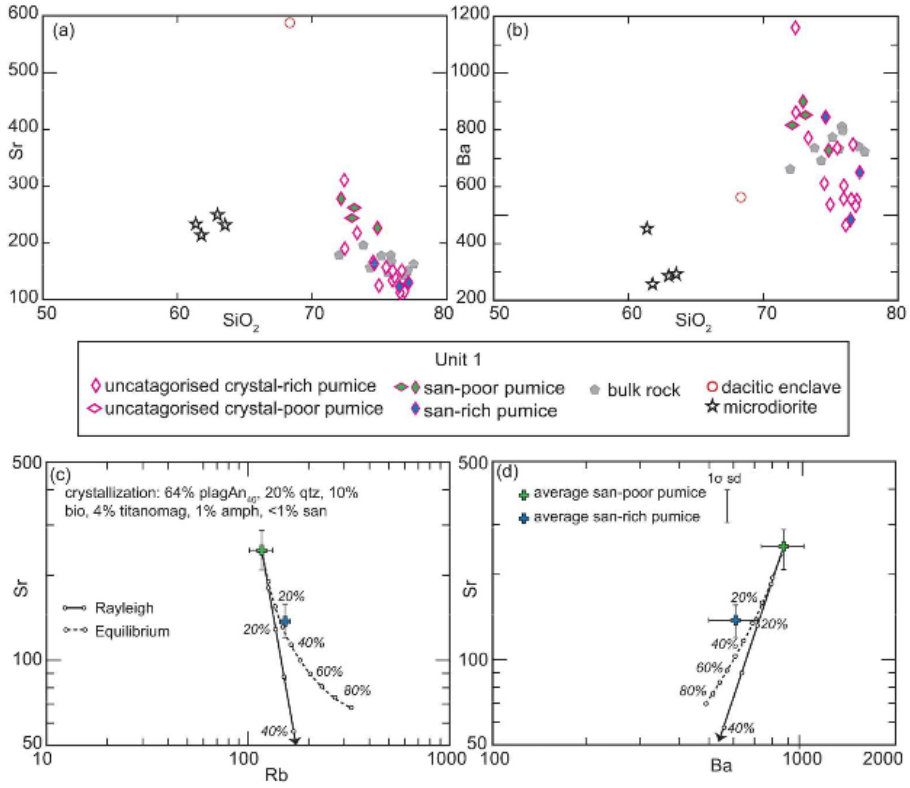

Trace elements

181x157mm (300 x 300 DPI)

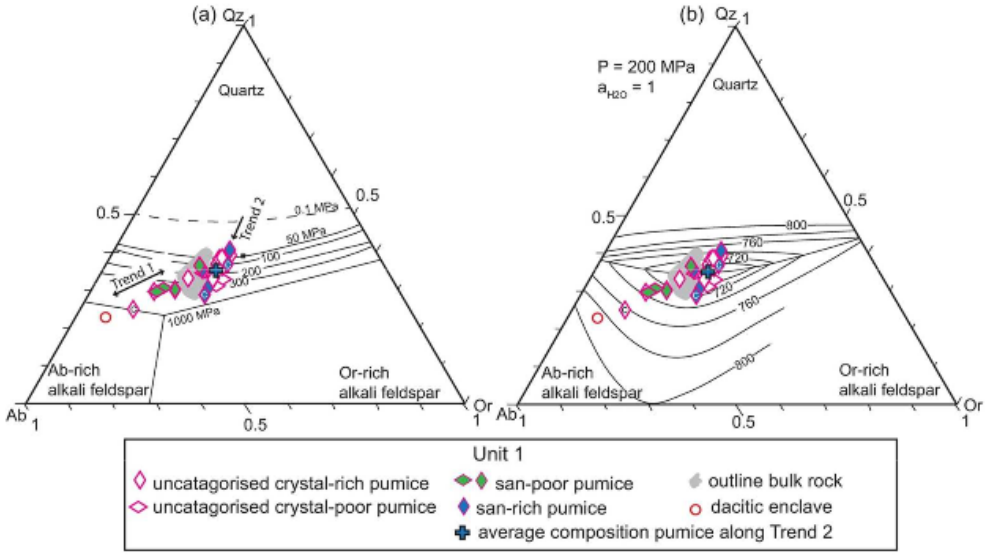

Figure 6. Qtz-Ab-Or Ternary diagrams

121x70mm (300 x 300 DPI)

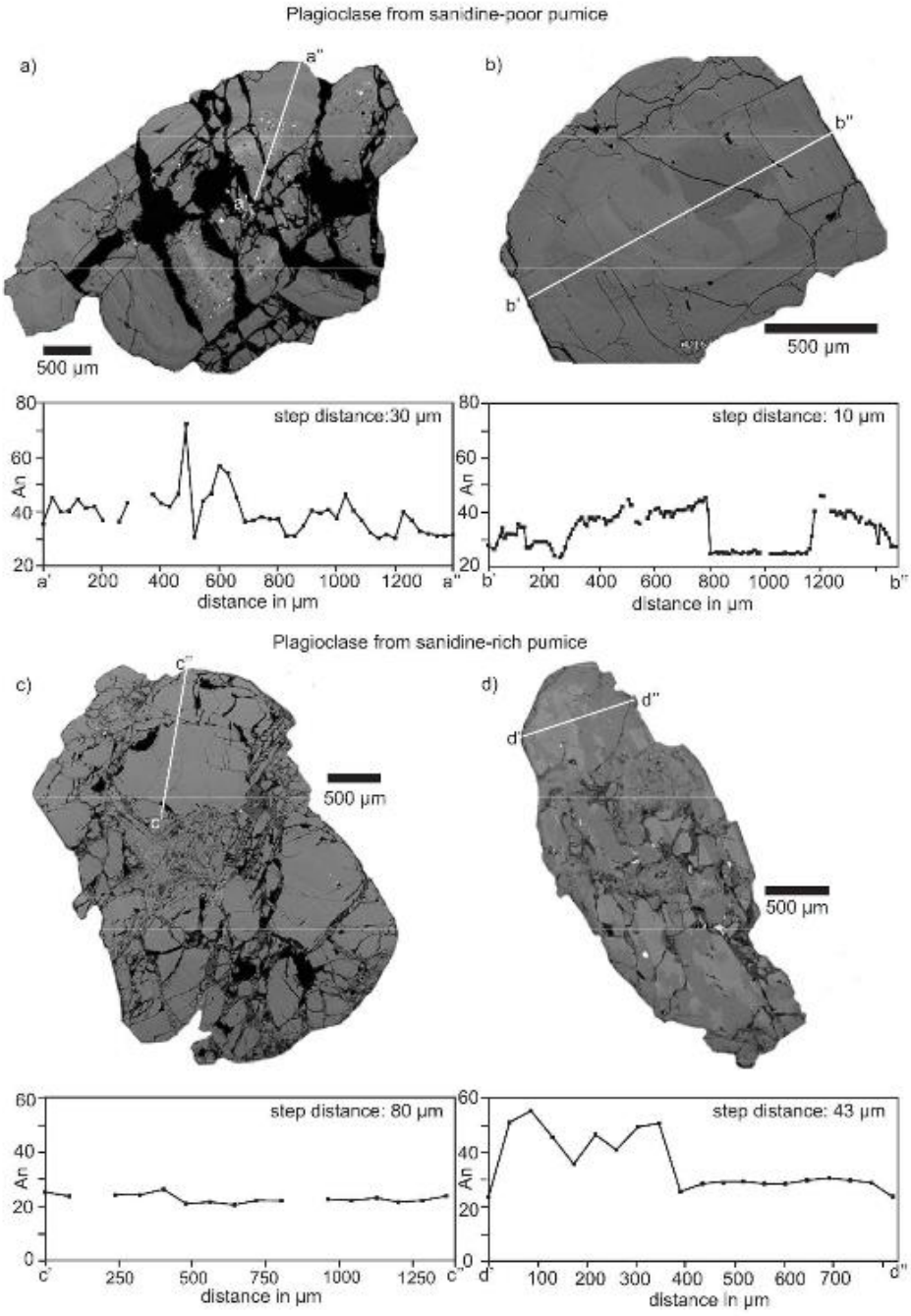

Figure 7. Plagioclase BSE-images and composition

298x427mm (300 x 300 DPI)

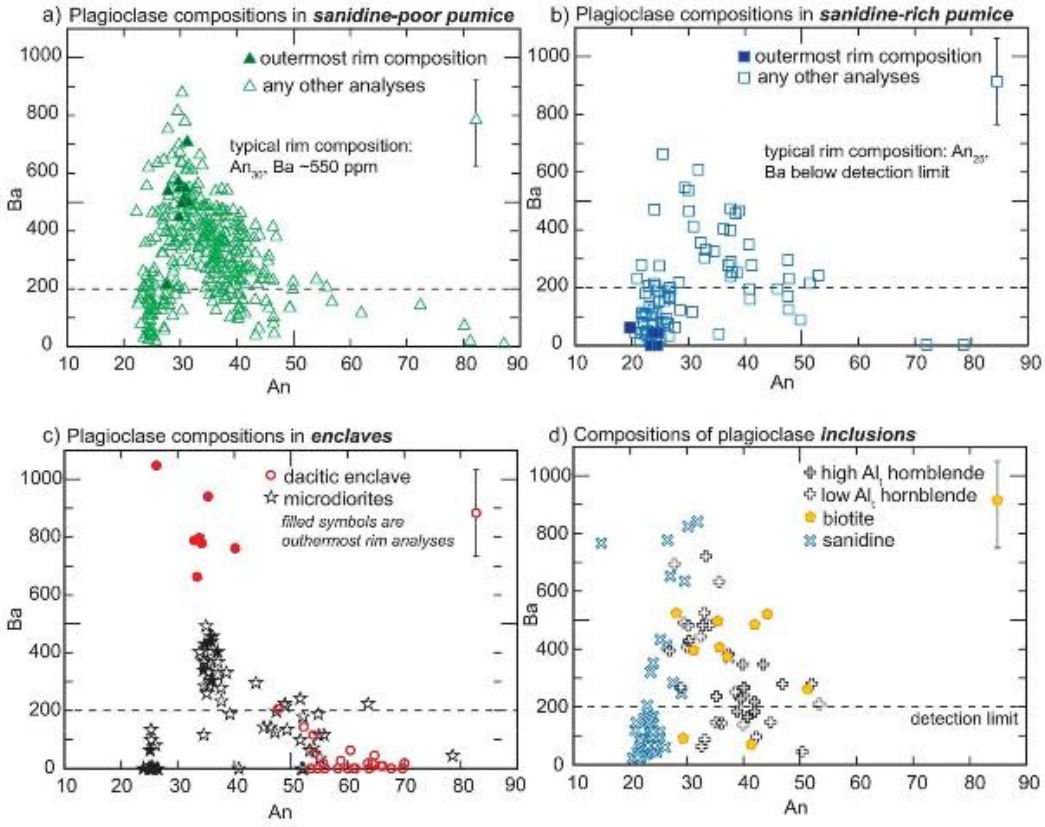

Figure 8. Plagioclase composition

166x127mm (300 x 300 DPI)

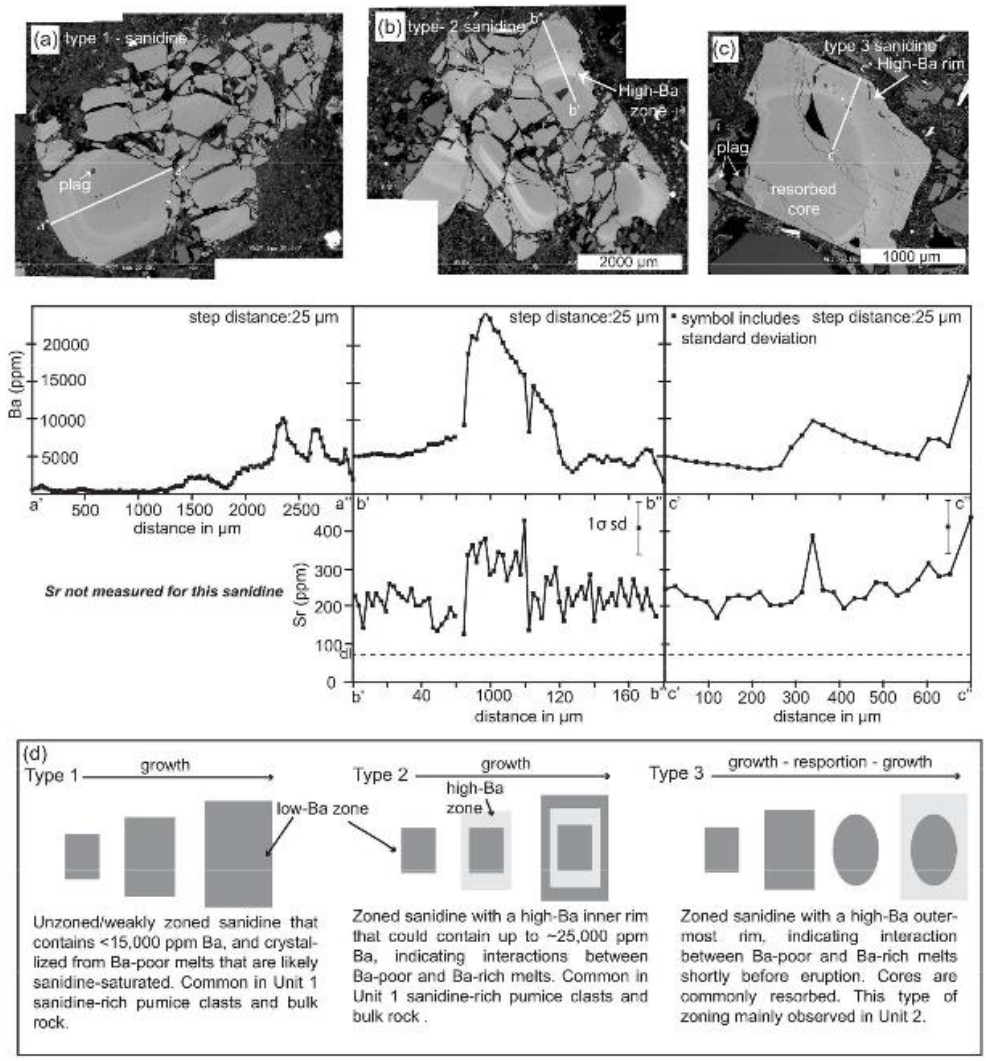

Figure 9. Sanidine BSE-images and composition

234x258mm (300 x 300 DPI)

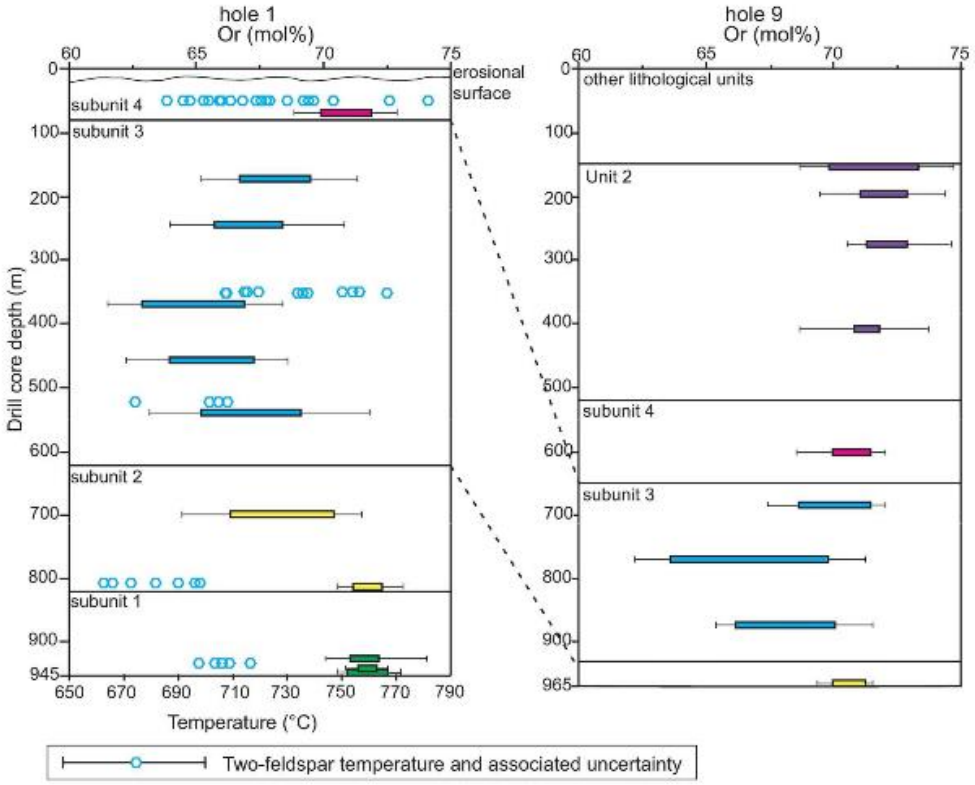

Figure 10. San Or-composition

187x173mm (300 x 300 DPI)

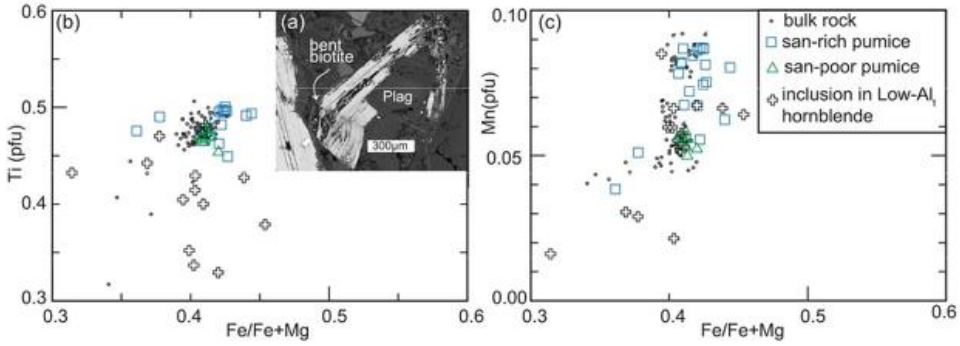

Figure 11. Biotite composition

72x25mm (300 x 300 DPI)

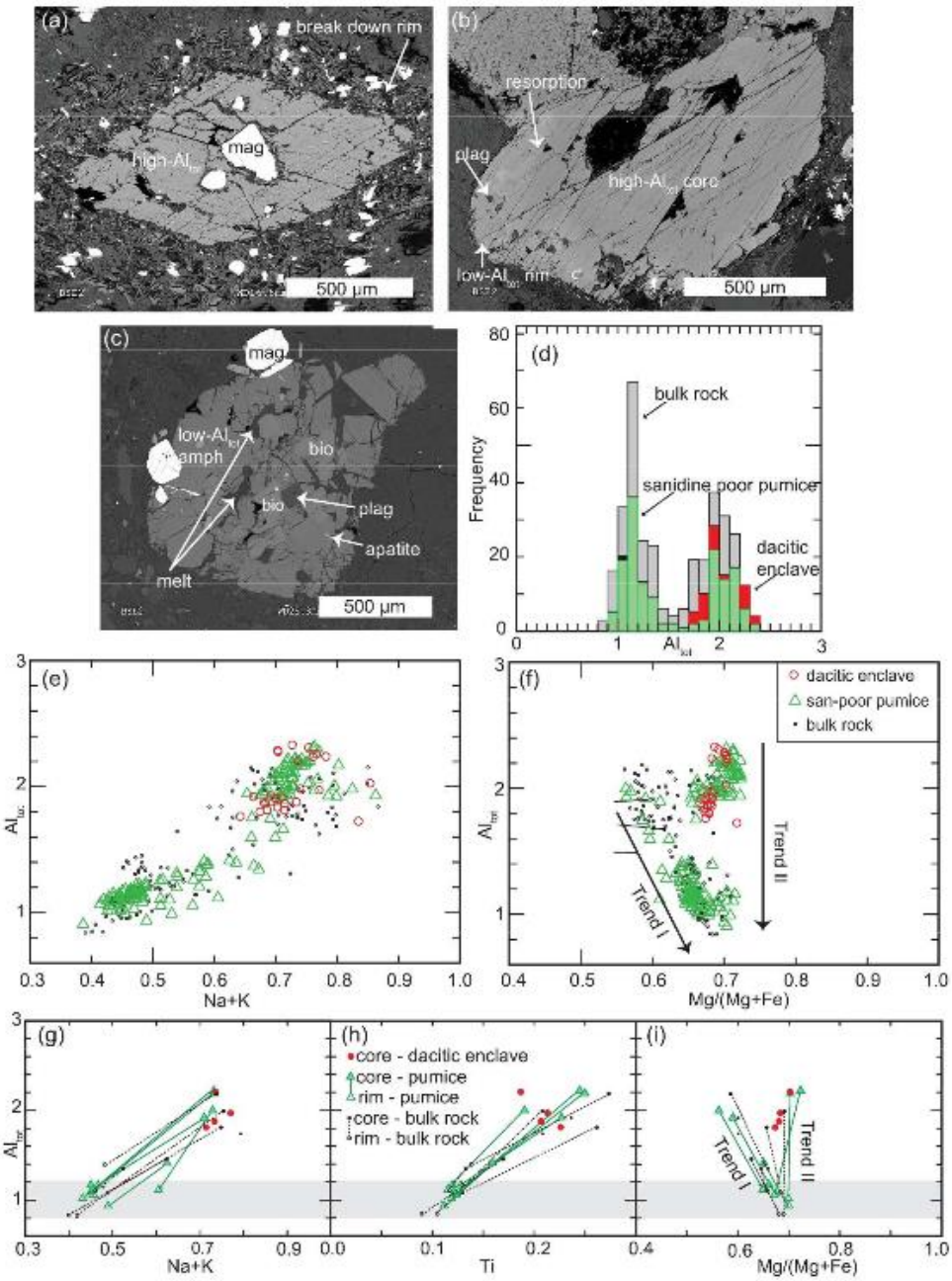

Amphibole composition

245x326mm (300 x 300 DPI)

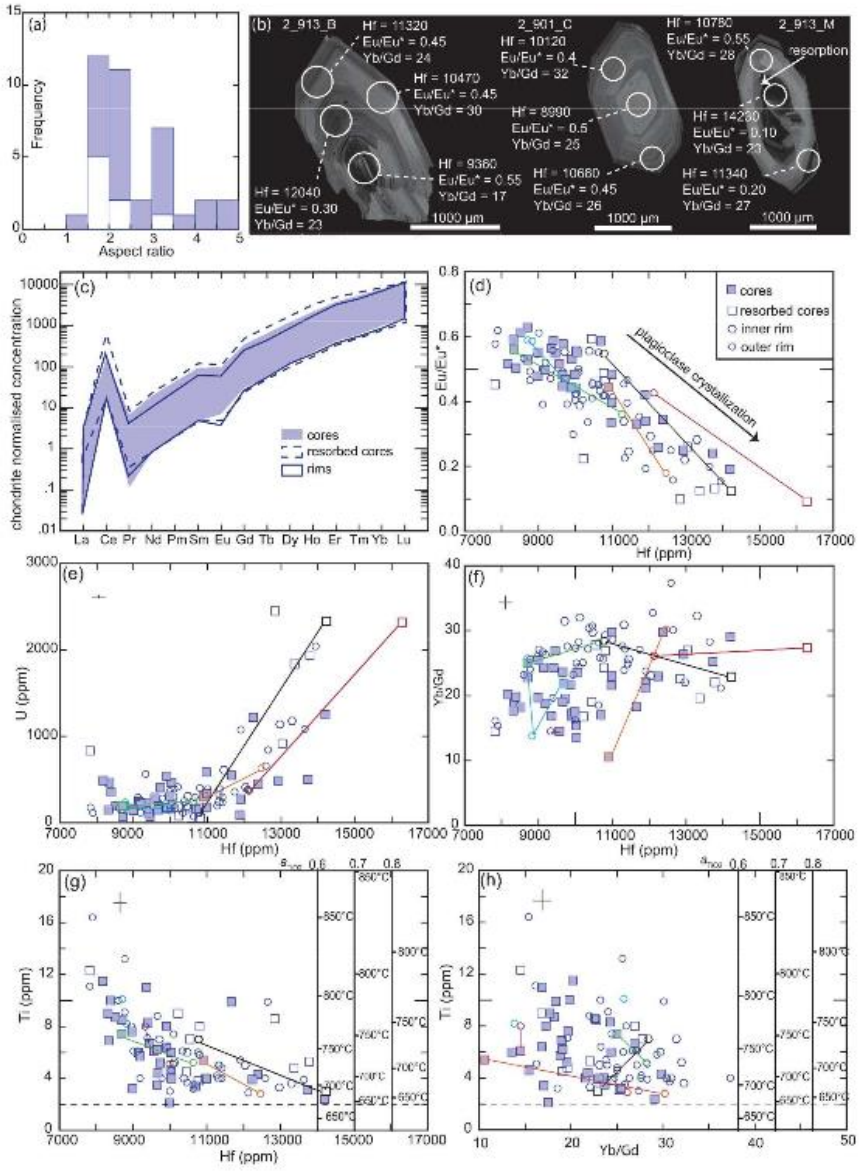

Figure 13. Zircon composition

286x366mm (300 x 300 DPI)

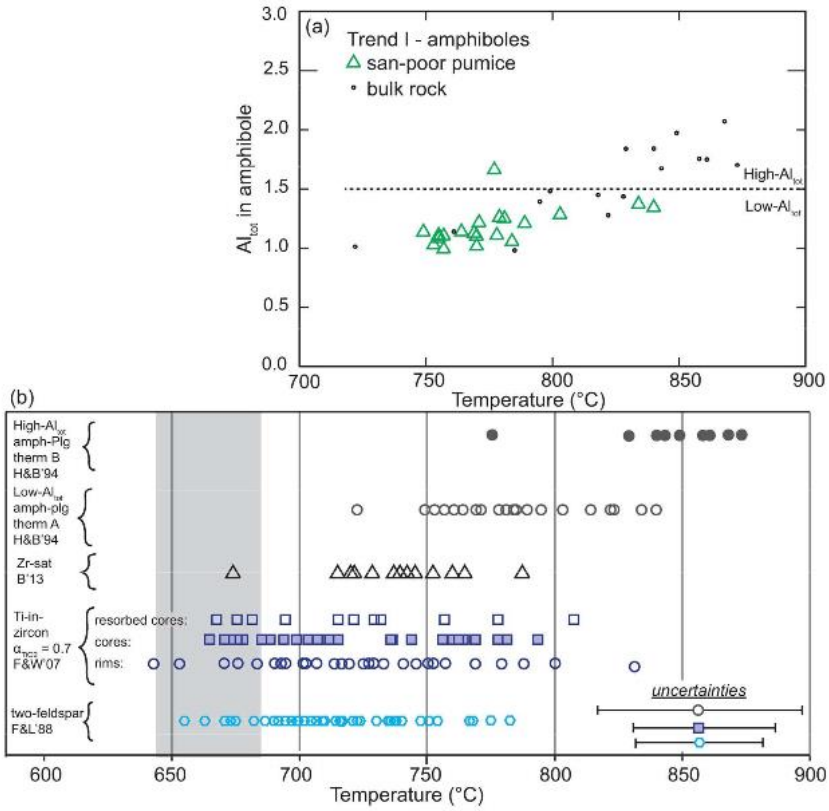

Thermometry

171x166mm (300 x 300 DPI)

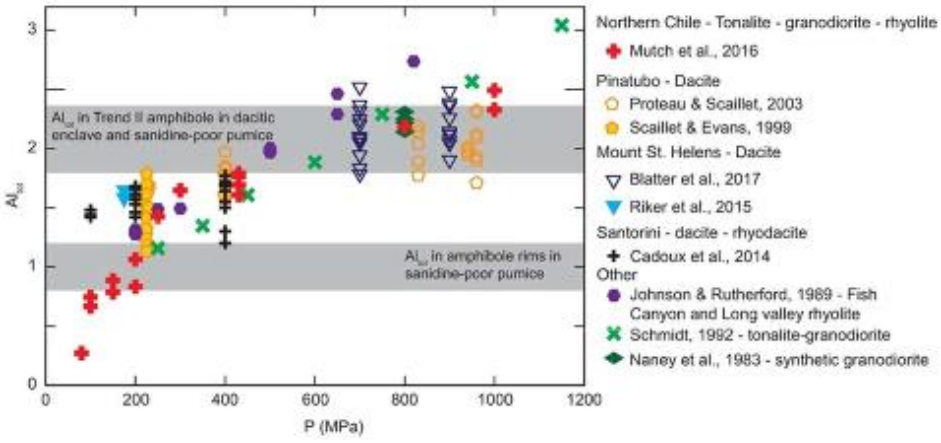

Pressure vs. Altot amphibole

93x32mm (300 x 300 DPI)

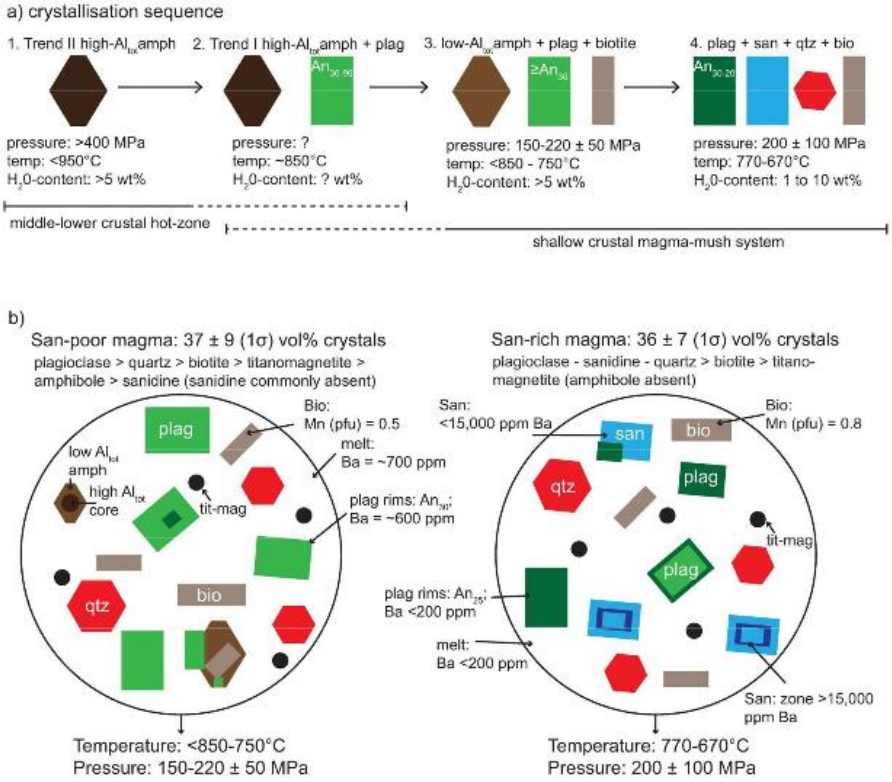

Crystallisation sequence

184x163mm (300 x 300 DPI)

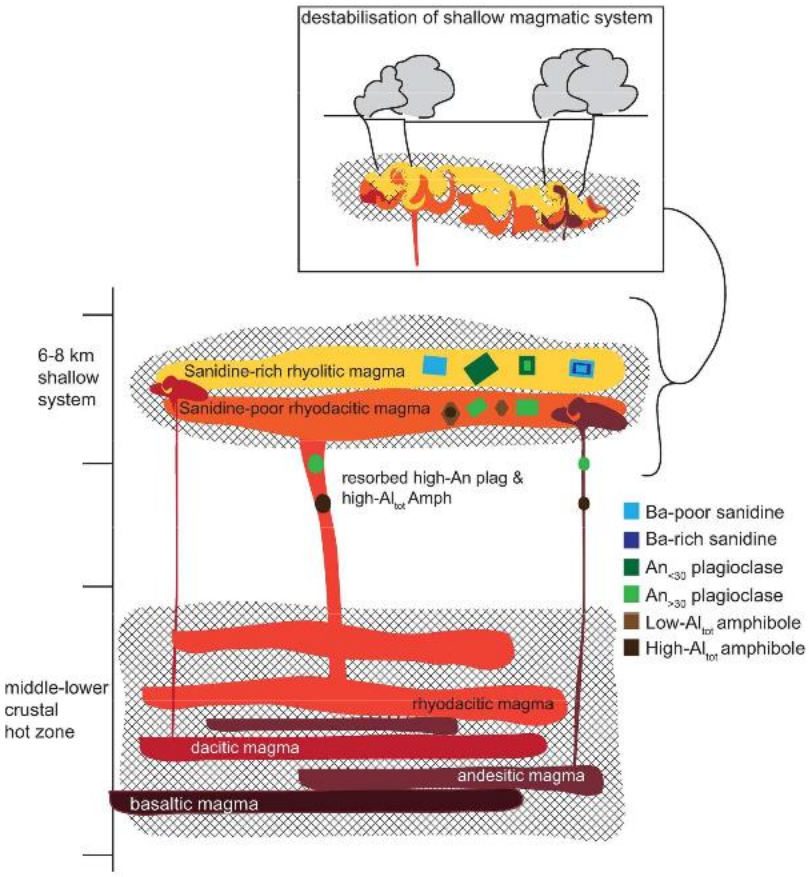

Magmatic model

199x207mm (300 x 300 DPI)